Atmos. Meas. Tech. Discuss., 6, 4769–4850, 2013
www.atmos-meas-tech-discuss.net/6/4769/2013/
doi:10.5194/amtd-6-4769-2013

Atmospheric Measurement Techniques Discussions

Carbon Monitoring Satellite (CarbonSat): assessment of scattering related atmospheric CO_2 and CH_4 retrieval errors and first results on implications for inferring city CO_2 emissions

M. Buchwitz[1], M. Reuter[1], H. Bovensmann[1], D. Pillai[1], J. Heymann[1], O. Schneising[1], V. Rozanov[1], T. Krings[1], J. P. Burrows[1], H. Boesch[2], C. Gerbig[3], Y. Meijer[4], and A. Löscher[4]

[1]Institute of Environmental Physics (IUP), University of Bremen FB1, Otto Hahn Allee 1, 28334 Bremen, Germany
[2]Department of Physics and Astronomy, University of Leicester, Leicester, UK
[3]Max-Planck-Institute for Biogeochemistry (MPI-BGC), Jena, Germany
[4]ESA ESTEC, Noordwijk, the Netherlands

Received: 24 April 2013 – Accepted: 17 May 2013 – Published: 31 May 2013

Correspondence to: M. Buchwitz (michael.buchwitz@iup.physik.uni-bremen.de)

Published by Copernicus Publications on behalf of the European Geosciences Union.

Abstract

Carbon Monitoring Satellite (CarbonSat) is one of two candidate missions for ESA's Earth Explorer 8 (EE8) satellite – the selected one to be launched around the end of this decade. The objective of the CarbonSat mission is to improve our understanding of natural and anthropogenic sources and sinks of the two most important anthropogenic greenhouse gases (GHG) carbon dioxide (CO_2) and methane (CH_4). The unique feature of CarbonSat is its "GHG imaging capability", which is achieved via a combination of high spatial resolution (2 km × 2 km) and good spatial coverage (wide swath and gap-free across- and along-track ground sampling). This capability enables global imaging of localized strong emission source such as cities, power plants, methane seeps, landfills and volcanos and better disentangling of natural and anthropogenic GHG sources and sinks. Source/sink information can be derived from the retrieved atmospheric column-averaged mole fractions of CO_2 and CH_4, i.e. XCO_2 and XCH_4, via inverse modeling. Using the most recent instrument and mission specification, an error analysis has been performed using the BESD/C retrieval algorithm. We focus on systematic errors due to aerosols and thin cirrus clouds, as this is the dominating error source especially with respect to XCO_2 systematic errors. To compute the errors for each single CarbonSat observation in a one year time period, we have developed an error parameterization scheme based on six relevant input parameters: we consider solar zenith angle, surface albedo in two bands, aerosol and cirrus optical depth, and cirrus altitude variations but neglect, for example, aerosol type variations. Using this method we have generated and analyzed one year of simulated CarbonSat observations. Using this data set we estimate that scattering related systematic errors are mostly (approx. 85 %) below 0.3 ppm for XCO_2 (< 0.5 ppm: 99.5 %) and below 2 ppb for XCH_4 (< 4 ppb: 99.3 %). We also show that the single measurement precision is typically around 1.2 ppm for XCO_2 and 7 ppb for XCH_4 (1-sigma). The number of quality filtered observations over cloud and ice free land surfaces is in the range 33–47 million per month depending on month. Recently it has been shown that terrestrial Vegetation

AMTD
6, 4769–4850, 2013

Chlorophyll Fluorescence (VCF) emission needs to be considered for accurate XCO_2 retrieval. We therefore retrieve VCF from clear Fraunhofer lines located at 755 nm and show that CarbonSat will provide valuable information on VCF. The VCF single measurement precision is approximately 0.3 mW m^{-2} nm^{-1} sr^{-1} (1-sigma). As a first application of the one year data set we assess the capability of CarbonSat to quantify the CO_2 emissions of large cities using Berlin, the capital of Germany, as an example. We show that the precision of the inferred Berlin CO_2 emissions as obtained from single CarbonSat overpasses is in the range 5–10 Mt CO_2 yr^{-1} (10–20 %). We found that systematic errors could be on the same order depending on which assumptions are used with respect to observational and biogenic XCO_2 modeling errors.

1 Introduction

Carbon dioxide (CO_2) and methane (CH_4) are the two most important anthropogenic greenhouse gases (GHG) contributing to global warming (Solomon et al., 2007). Their concentration in the atmosphere significantly increased during the previous decades and still continues to increase (e.g. Francey et al., 2013; Olivier et al., 2012; Schneising et al., 2011; Dlugokencky et al., 2009, and references given therein). Despite their importance, our knowledge on their sources and sinks has significant gaps (e.g. Canadell et al., 2010; Rigby et al., 2008; Stephens et al., 2007).

Global satellite observations of CO_2 and CH_4 can help to close important knowledge gaps on CO_2 and CH_4 regional-scale sources and sinks (e.g. Guerlet et al., 2013a; Basu et al., 2013; Maksyutov et al., 2012; Bergamaschi et al., 2009; Rayner and O'Brien, 2001). Knowledge gaps also exist on smaller scales, e.g. for CO_2 emitting power plants (e.g. Krings et al., 2011; Velazco et al., 2011; Bovensmann et al., 2010, and references given therein), CO_2 emissions from cities or large urban agglomerations (e.g. Schneising et al., 2013, 2008; Keppel-Aleks et al., 2012; Kort et al., 2012, and references given therein), and various local industrial and geological sources of methane (e.g. Krings et al., 2013; Leifer et al., 2013; Bovensmann et al., 2010, and references

AMTD
6, 4769–4850, 2013

given therein). Satellite observations of greenhouse gases are also required to contribute to the verification of international climate agreements (e.g. NRC, 2010, and references given therein).

These applications require high precision and accuracy, good spatio-temporal coverage and sensitivity to near-surface concentration variations (e.g. Buchwitz et al., 2011, 2013; Chevallier et al., 2007; Meirink et al., 2006). The Carbon Monitoring Satellite (CarbonSat) (Bovensmann et al., 2010) mission and instrument concept is addressing these needs. The objective of the CarbonSat mission is to determine and separate natural and anthropogenic CO_2 and CH_4 sources and sinks. CarbonSat will contribute to the quantification of natural fluxes of CO_2 and CH_4 (e.g. biospheric CO_2, wetland CH_4) but also to a much better estimation of anthropogenic emissions than possible with any of the other existing or planned satellite missions. This will be achieved via a unique feature of CarbonSat, which is its "GHG imaging capability". GHG imaging is achieved via a combination of high spatial resolution (2 km × 2 km) and good spatial coverage achieved by a relatively wide swath and no gaps between adjacent (across-track and along-track) ground pixel. The width of the across-track swath has not yet been finally decided. Here we present results for two swath widths: 240 km (CarbonSat's breakthrough requirement) and 500 km (goal requirement). This capability enables global imaging of localized strong emission sources such as cities, power plants, methane seeps, landfills and volcanos and a better disentangling of anthropogenic and GHG natural sources and sinks.

The main data products of CarbonSat are atmospheric column-averaged dry-air mole fractions of CO_2 and CH_4, denoted XCO_2 and XCH_4. These data products are also generated or are planned to be generated, from other past, present and future greenhouse gas missions such as SCIAMACHY (Burrows et al., 1995; Bovensmann et al., 1999; Buchwitz et al., 2005), GOSAT (Kuze et al., 2009; Yoshida et al., 2011) and the upcoming OCO-2 mission (XCO_2 only) (Crisp et al., 2004; Boesch et al., 2011). Compared to these missions, CarbonSat aims at better disentangling natural and anthropogenic sources and sinks of CO_2 and CH_4 due to its GHG imaging capability.

AMTD
6, 4769–4850, 2013

CarbonSat has been selected by the European Space Agency (ESA) to be one of two candidate missions for ESA's Earth Explorer 8 (EE8) satellite. The other candidate mission is the FLuorscence EXplorer (FLEX) (Rascher, 2007; ESA, 2008). The selected mission will be launched around the end of this decade (i.e. around 2020).

Near-surface sensitivity is achieved by measuring spectra of solar radiation reflected at the Earth's surface and backscattered into the atmosphere to space using spectral regions sensitive to CO_2 and CH_4 absorption. These spectra are also influenced by atmospheric scattering by air molecules (Rayleigh scattering), aerosols and clouds. Scattering influences the light path and needs to be appropriately considered when retrieving CO_2 and CH_4 information from the measured spectra. The focus of this manuscript is to address this aspect. It is well known that unaccounted variability of atmospheric scattering by aerosols and clouds, especially undetected thin cirrus clouds, are a major error source for satellite CO_2 and CH_4 retrieval in the solar spectral region (e.g. Guerlet et al., 2013b; Heymann et al., 2012a,b; Oshchepkov et al., 2012; O'Dell et al., 2012; Reuter et al., 2011; Butz et al., 2011). It is therefore important to assess to what extent a particular type of measurement (here the proposed measurements of CarbonSat) may suffer from this error source. To evaluate this, we have conducted an assessment based on simulated CarbonSat observations. We focus on errors due to aerosols and cirrus clouds assuming that scenes contaminated by thick clouds have already been identified (e.g. by pre-processing O_2 A-band spectra) and removed (similar to that currently done for SCIAMACHY (e.g. Heymann et al., 2012a,b; Reuter et al., 2011) and GOSAT (e.g. Cogan et al., 2012; O'Dell et al., 2012; Crisp et al., 2012; Butz et al., 2011).

Initial error analysis results for CarbonSat concerning aerosols and cirrus clouds have already been presented in Bovensmann et al. (2010), focusing on one application, namely to infer CO_2 emissions of coal-fired power plants from single overpass CarbonSat XCO_2 observations. Here we extend this analysis by computing and analyzing errors for one year of global simulated CarbonSat observations. For this purpose we have developed an error parameterization method which permits fast computation

AMTD
6, 4769–4850, 2013

of random and systematic XCO_2 and XCH_4 errors as a function of several critical input parameters such as aerosol Optical Depth (OD), cirrus OD and cirrus altitude. The error analysis is based on the most recent instrument and mission specification and uses the latest version of the BESD/C "full physics" algorithm (Bovensmann et al., 2010) for retrieving geophysical parameters from CarbonSat radiances.

This manuscript is structured as follows: in Sect. 2 the CarbonSat instrument concept is described and in Sect. 3 the retrieval algorithm is briefly presented focusing on recent improvements. In Sect. 4 the error analysis and error parameterization approach is described. The error parameterization method permits fast computation of random and systematic XCO_2 and XCH_4 errors and averaging kernels and has been used to generate one year of simulated CarbonSat observations. How this data set has been generated is described in Sect. 5. As a first application the data set is used to assess to what extent CarbonSat can quantify the anthropogenic CO_2 emissions of cities using Berlin as an example (Sect. 6). This assessment is based on single Berlin overpass data by analyzing CarbonSat derived "XCO_2 images". In Sect. 7, an analysis of the global data is presented. This comprises spatio-temporally averages and assessments for various regions as relevant for the application to quantify natural CO_2 and CH_4 fluxes on regional scales. Limitations of our approach and an outlook to future work are shortly discussed in Sect. 8. A summary and conclusions are given in Sect. 9.

2 CarbonSat mission and instrument concept

CarbonSat aims to deliver XCO_2 (in ppm) and XCH_4 (in ppb) at a high spatial resolution of 2 km × 2 km and good spatial coverage via continuous imaging across a 240 km swath width (CarbonSat's "breakthrough requirement"; the more demanding "goal requirement" is 500 km). The orbit will be sun-synchronous. For this study we assume that the orbit will be similar to NASA's Terra satellite (www.nasa.gov/terra/) but with an equator crossing time of 11.30 a.m. (Local Time Descending Node – LTDN). CarbonSat's main mode will be the nadir (downlooking) mode. CarbonSat will also obtain

AMTD
6, 4769–4850, 2013

solar spectra and perform observation in sun-glint mode, especially to improve the quality of the observations over water and snow and ice covered land surfaces, which are poor reflectors in the Short-Wave-Infra-Red (SWIR) spectral region outside of sun-glint conditions. As the sun-glint observation strategy has not yet been finally decided and because the BESD/C retrieval algorithm has not yet been optimized for sun-glint conditions, the CarbonSat sun-glint observations are not considered in this study. Here we focus on nadir mode observations over snow and ice free land surfaces.

The CarbonSat imaging spectrometer will cover three spectral bands (Table 1). The Near-Infra-Red (NIR) band covers the O_2 A-band spectral region (747–773 nm) at 0.1 nm spectral resolution (approx. 1.7 cm^{-1}). This band permits one to obtain information on aerosols, clouds, surface pressure and Vegetation Chlorophyll Fluorescence (VCF). The first SWIR band (SWIR-1) covers the 1590–1675 nm spectral region at 0.3 nm spectral resolution (approx. 1.2 cm^{-1}). This spectral region contains important absorption bands of CO_2 and CH_4 but is otherwise quite transparent and therefore permits one to deliver information on CO_2 and CH_4 columns with high near-surface sensitivity. The "strong CO_2 band" SWIR-2 covers the 1925–2095 nm region with spectral resolution of 0.55 nm (approx. 1.4 cm^{-1}). It contains additional information on CO_2 but also on water vapor and cirrus clouds, the latter from the saturated water band located at 1940 nm. The basic idea is to retrieve CO_2 and CH_4 columns from the transparent SWIR-1 band but to use in addition the partly non-transparent NIR and SWIR-2 bands located at smaller (NIR) and longer (SWIR-2) wavelengths to obtain information on atmospheric scatterers at 0.76 µm (NIR) and 2 µm (SWIR-2) to constrain the CO_2 and CH_4 retrieval at 1.6 µm (SWIR-1). In practice, all the needed information will essentially be retrieved simultaneously by applying an appropriate retrieval algorithm to all three bands (see Sect. 3).

For this study we use the latest specification of the CarbonSat imaging spectrometer currently available. Some further optimization of instrument requirements might be possible during mission development. The CarbonSat instrument specification as used for this study is similar but not exactly identical as the one described in Bovensmann et al.

AMTD
6, 4769–4850, 2013

(2010). The most relevant differences are: (i) the spectral resolution is somewhat lower compared to that assumed in Bovensmann et al. (2010), esp. in the NIR and SWIR-2 bands, driven by reduction in instrument complexity; (ii) the spectral coverage has been enlarged for the NIR band to include more clear Fraunhofer lines as recommended by Frankenberg et al. (2012), and also for the SWIR-2 band to cover a saturated water band at 1940 nm for improved cirrus detection similar as also done for SCIAMACHY (Heymann et al., 2012b) and GOSAT (Guerlet et al., 2013b); and (iii) the signal-to-noise ratio (SNR) has been enhanced to compensate for the reduced spectral resolution. For this study we use the required threshold (i.e. minimum) SNR performance of CarbonSat (see Table 1) and not, as in Bovensmann et al. (2010), a SNR model.

The instrument parameters (Table 1) are used by a CarbonSat instrument model, which converts high spectral resolution spectra as computed with the radiative transfer model SCIATRAN (Rozanov et al., 2005; Rozanov and Kokhanovsky, 2006) into simulated CarbonSat observations taking into account the relevant instrument characteristics as listed in Table 1. As an example, Fig. 1 shows a simulated CarbonSat nadir radiance spectrum, the solar irradiance, the corresponding sun-normalized radiance and signal-to-noise ratio (SNR) spectra for a scene with vegetation albedo (NIR: 0.2, SWIR-1: 0.1, SWIR-2: 0.05) and a solar zenith angle (SZA) of 50°.

3 BESD/C retrieval algorithm description

For this study the BESD/C retrieval algorithm (Bovensmann et al., 2010) has been used. The acronym BESD stands for "Bremen optimal EStimation DOAS". BESD/C retrieves XCO_2 and XCH_4 and additional parameters (e.g. for aerosols and cirrus clouds) from a simultaneous analysis of the three CarbonSat bands NIR, SWIR-1 and SWIR-2. BESD/C is described in detail in Bovensmann et al. (2010). Therefore we here give only a short overview focusing on recent improvements.

AMTD
6, 4769–4850, 2013

3.1 General description

BESD/C is similar but not exactly identical to the BESD algorithm used for SCIAMACHY XCO_2 retrieval (Reuter et al., 2010, 2011). BESD/C and BESD are "full physics" (FP) retrieval algorithms. As shown in Bovensmann et al. (2010), BESD/C also permits one to perform "proxy" (PR) retrievals. BESD/C retrieves CO_2 and CH_4 vertical columns (in molecules per cm^2), which are converted into dry air column-averaged mole fractions or mixing ratios, i.e. XCO_2 (in ppm) and XCH_4 (in ppb), by dividing the retrieved GHG columns by the dry air column (in number of air molecules, except water vapor, per cm^2). For a FP algorithm, the (dry) air column is obtained from retrieved surface pressure, e.g. obtained from the O_2 A-band spectral region, or from surface pressure obtained from meteorological analysis fields (corrected for water vapor using retrieved or meteorologically analyzed water vapor columns). Essentially both sources of information are used to compute the dry air column as the retrieval will use meteorological information as first guess and a priori information. For a PR algorithm, the air column is obtained from a reference gas, which is CO_2 in case of PR XCH_4 (e.g. Frankenberg et al., 2005; Schneising et al., 2011; Krings et al., 2013) or CH_4 in case of PR XCO_2 (see Bovensmann et al., 2010; Krings et al., 2011). The reference gas should be less variable than the target gas (or can be modelled with sufficient accuracy). Typically PR retrievals require a correction procedure for variations of the reference gas using a model (see also Schepers et al., 2012), for a discussion of FP versus PR retrievals). If a PR method can be used depends on the application, whereas the FP method is always applicable as it does not require any assumptions on the reference gas. In this study we focus on FP retrievals and discuss PR retrievals only briefly. Despite the mentioned limitations, PR retrievals have the advantage that systematic errors caused by, e.g. clouds and aerosols, cancel to a large extent when the GHG column ratio is computed (we illustrate this using one example). For some applications (e.g. Bovensmann et al., 2010; Krings et al., 2011, 2013) this is advantageous as it enhances the accuracy.

AMTD
6, 4769–4850, 2013

BESD/C is based on "Optimal Estimation" (OE) (Rodgers, 2000) and uses a priori information to constrain the retrieval. BESD/C has already been applied to simulated CarbonSat observations as shown in Bovensmann et al. (2010). In that publication BESD/C has been used via a fast non-iterative look-up-table approach. For the results presented here, BESD/C has been improved to enhance the accuracy. This has been achieved by fully coupling BESD/C to the radiative transfer model (RTM) SCIATRAN (Rozanov et al., 2005; Rozanov and Kokhanovsky, 2006) as this permits an iterative retrieval by calling the RTM with updated parameters after each iteration step. During the iteration, the BESD cost function (see Eq. 7, Bovensmann et al., 2010) is minimized. The method used to minimize the cost function is based on Levenberg–Marquardt and is identical for BESD and BESD/C and described in Reuter et al. (2011). This (or an equivalent) iterative procedure improves the accuracy of the retrieved XCO_2 and XCH_4 in the presence of variable (and unknown) amounts of aerosols and cirrus clouds and is essentially the standard method also used by other algorithms (e.g. O'Dell et al., 2012; Butz et al., 2011; Reuter et al., 2010, 2011).

Compared to the BESD/C version described in Bovensmann et al. (2010), the BESD/C state vector, which contains all elements to be retrieved via the OE retrieval procedure, has been extended. All state vector elements are listed in Table 2. For each state vector element the derivative of the radiance with respect to the state vector element is needed to characterize the change of the radiance due to a change of that state vector element. These derivatives define the Jacobian matrix, which contains the derivative spectra in each of its columns (for the BESD/C Jacobian matrix, see matrix **K** described in Bovensmann et al., 2010). For BESD/C the derivative spectra are computed (quasi-analytically) by SCIATRAN. A typical BESD/C Jacobian matrix as used for this study is shown in Fig. 2. Note that each spectrum has been scaled such that the spectra do not overlap in this figure and that it is not possible to see all relevant details in Fig. 2. For example, for AOD retrieval, two Jacobians are shown, namely "AODNIR" and "AODSW2". AODNIR covers the NIR and SWIR-1 bands (and is zero in the SWIR-2 band), whereas AODSW2 covers the SWIR-2 and SWIR-1 bands (an is

AMTD
6, 4769–4850, 2013

zero in the NIR band). The spectral variations of these two Jacobians in the SWIR-1 band are difficult to see in this figure as the amplitude of these Jacobians is much larger in the two "strongly absorbing" NIR and SWIR-2 bands (in the NIR due to strong O_2 absorption; in the SWIR-2 due to strong CO_2 and H_2O absorption). This indicates that AOD information can primarily be derived (only) from the NIR and SWIR-2 bands. The coupling with the SWIR-1 band ensures (at least to some extent) that AOD information obtained from the NIR and SWIR-2 bands is "made available" in the SWIR-1 band (the AOD information content of SWIR-1 band is negligible, especially if only "differential" information is used – BESD/C DOAS polynomial, as the AOD Jacobian correlates with other Jacobians, e.g. with the CO_2 Jacobian).

BESD/C as described here has been applied to a number of scenarios to quantify random and systematic XCO_2 and XCH_4 errors. Results of this exercise are presented and discussed in Sect. 4 focusing on aerosol and cirrus related errors. Before the error analysis results are presented we discuss one additional aspect, namely how to consider potential issues related to Vegetation Chlorophyll Fluorescence (VCF) emission, which also needs to be considered, as it influences the radiance in the NIR band of CarbonSat.

3.2 Consideration of terrestrial Vegetation Chlorophyll Fluorescence (VCF)

Recently it has been shown that terrestrial Vegetation Chlorophyll Fluorescence (VCF) emission needs to be considered for accurate XCO_2 retrieval (Frankenberg et al., 2012). BESD/C has therefore been improved to consider this. As can be seen from Table 2, VCF is a state vector element for the version of BESD/C used in this study. In order to provide the radiative transfer model with a reasonable VCF first guess value, a simple but very fast "Dedicated VCF" (DVCF) retrieval scheme has been implemented. It is not based on full SCIATRAN computations but uses only a few constant pre-computed spectra (plus a low order polynomial) to model the sun-normalized radiance via scaling these spectra using a simple but fast OE retrieval scheme. The method

AMTD
6, 4769–4850, 2013

we use is similar to the methods described in Joiner et al. (2011) and Frankenberg et al. (2011).

The following spectra are used for DVCF pre-processing:

- A high spectral resolution solar irradiance spectrum. We use the "OCO Toon spectrum" described in O'Dell et al. (2012). This spectrum is the most important spectrum as required for VCF retrieval based on clear solar Fraunhofer lines.
- A low order polynomial to consider spectrally broad-band radiance variations due to, e.g. aerosols, clouds and surface albedo or residual calibration issues.
- A surface emission VCF spectrum (Rascher et al., 2009). Note however that only a small spectral region is used by the DVCF algorithm (749–759 nm) and that the VCF spectrum is essentially constant (or varies only linearly) in this narrow spectral range and that therefore the retrieval results are essentially independent of the VCF spectrum used.
- A water vapor absorption spectrum computed off-line with SCIATRAN using HITRAN 2008 spectroscopic line parameters (Rothman et al., 2009). Note that the underlying water absorption in the DVCF retrieval window is very weak and that including water absorption only slightly improves the quality of the spectral fit but hardly changes the retrieved VCF values.

These spectra are used at present by a simple but very fast non-iterative OE scheme to retrieve VCF essentially as a scaling factor of the VCF Jacobian. Atmospheric absorption and scattering are neglected by the currently implemented DVCF retrieval method.

A DVCF example fit is shown in Fig. 3. The CarbonSat nadir radiance (L, top panel a, black line) has been computed with the latest version of the SCIATRAN radiative transfer model, which takes all relevant processes including (multiple) scattering and surface emission by VCF into account. As can be concluded from the similarity between the (scaled) solar irradiance (F, top panel, red line) and the (scaled) nadir radiance, the

AMTD
6, 4769–4850, 2013

spectral region used for DVCF retrieval is essentially free of atmospheric absorption features (even water vapor absorption is very small in this region). The difference between the two (scaled) spectra is primarily due to terrestrial vegetation fluorescence emission at the surface, which causes a (tiny) filling-in of the solar Fraunhofer lines (most clearly seen for the two strongest lines located at 749.7 and 751.3 nm) and a slope change over the spectral region (note that L and F have seen scaled to 1.0 at the lowest wavelength shown in Fig. 3). Panel b of Fig. 3 shows the corresponding sun-normalized radiance (black line) and its measurement error (1-sigma noise level, grey vertical bars) and the fitted simple DVCF model (red line). As can be seen, the fit is good but not perfect. Especially the amplitude of the peaks do not match perfectly. This is due to the currently used fast and simple (e.g. non-iterative) DVCF model, which is not based on the full VCF Jacobian computed by SCIATRAN (note that SCIATRAN is not used for the DVCF retrieval). As a result, the retrieved VCF is somewhat underestimated for VCF values larger than the used a priori value (of 0.8 $\mathrm{mW\,m^{-2}\,nm^{-1}\,sr^{-1}}$) and overestimated for VCF values less than the used a priori value (at the a priori value the error is zero). The deviation is to a good approximation linear and scenario independent and therefore a simple linear correction is used. This can be improved using a more advanced algorithm, e.g. by using SCIATRAN for DVCF retrieval, but this would require more computational resources. For the purpose of this study, the currently implemented fast DVCF retrieval method is used. The retrieved VCF is used as a first guess and a priori value for the full 3-band BESD/C retrieval.

The DVCF retrieval method has been used to retrieve VCF from a large number of scenarios taking into account different SZA, aerosol amounts and cirrus parameters. Figure 4 shows the results for 180 scenarios (the parameters which have been varied are listed in Fig. 4, see blue text in panel a). As can be seen, a very good correlation between the retrieved and the true VCF exists ($r = 0.99$). As can also be seen, the standard deviation of the difference is 0.19 $\mathrm{mW\,m^{-2}\,nm^{-1}\,sr^{-1}}$ (less than approx. 20 % except for very low VCF emission (see panel b). Also listed is the single observation

AMTD
6, 4769–4850, 2013

retrieval precision, which is $0.233 \pm 0.031\,\mathrm{mW\,m^{-2}\,nm^{-1}\,sr^{-1}}$ (mean and standard deviation as obtained from all 180 scenarios).

4 XCO_2 and XCH_4 error analysis and parameterization

In this section we present and discuss our error analysis and error parameterization approach for scattering related errors. We focus on systematic XCO_2 and XCH_4 retrieval errors but also discuss random errors due to instrument noise. There are several other error sources, such as residual calibration errors, which contribute to systematic (and random or quasi random) errors. These error sources have been considered when formulating the CarbonSat mission and instrument requirements but are not discussed here. The main goal of the error parameterization described here is to compute random and scattering related systematic errors for each single CarbonSat observation for a one year time period. Due to the large number of CarbonSat observations, this requires an approriate, i.e. very fast but sufficiently accurate, scheme to compute these errors. How this has been achieved is described in the following.

4.1 General considerations

Systematic retrieval errors especially for scattering parameters depend significantly on parameters such as the amount of aerosol (characterized by, e.g. Aerosol Optical Depth, AOD, at the relevant wavelengths), Cirrus Optical Depth, COD, and altitude – Cirrus Top Height, CTH) and surface spectral reflectance (characterized by, e.g. Lambertian surface albedo). An initial error analysis of CarbonSat XCO_2 and XCH_4 errors due to aerosols and clouds has already been presented in Bovensmann et al. (2010), focusing on CarbonSat power plant overpasses. Here we present an extension of that analysis to assess the quality of the global data. We aim at estimating random and systematic XCO_2 and XCH_4 errors for one year of CarbonSat global observations. Ideally, this should be done by applying the retrieval algorithm to all individual observations.

AMTD
6, 4769–4850, 2013

However, due to the large amounts of data, CarbonSat will generate, and because the retrieval program BESD/C as currently implemented is quite slow, this is not yet possible. Reducing the processing time is an important task for the future. For the purpose of this study we have developed an error parameterization scheme, which is described in this section. This scheme permits one to compute the XCO_2 and XCH_4 errors as a function of several scattering related critical input parameters. A similar approach has also been used by Hungershoefer et al. (2010) to assess the impact of satellite XCO_2 errors for CO_2 surface flux inversions.

The goal of this study is to realistically estimate the expected CarbonSat performance in terms of XCO_2 and XCH_4 random and systematic errors. Random errors are primarily determined by the instrument signal-to-noise performance. It is believed that random errors can be reliably quantified already at this early stage (note that the instrument design is still being optimized) assuming, for example, that detectors will not dramatically improve in the near future. Systematic errors however also depend critically on the retrieval algorithm and its parameter settings. It is expected that the BESD/C algorithm will be significantly further improved in the coming years, e.g. by better exploiting the strong water band in the 1940 nm spectral region for cirrus detection (e.g. Heymann et al., 2012b), or by further improving the aerosol retrieval method by also retrieving an aerosol size parameter (e.g. Butz et al., 2011). One way to consider future improvements could be to reduce systematic errors by a certain factor. Such a factor can however not be reliably estimated. For this study we use BESD/C as is. However, we solve a somewhat simplified retrieval problem, e.g. by focusing only on a few parameters, which are known to be critical ones. Our approach is more advanced than the relatively simple approach for other dedicated GHG satellite missions as used by Hungershoefer et al. (2010), as we consider more parameters, but it is still quite simple, as we neglect, for example, microphysical parameter variations for aerosols (this aspect is further discussed in Sect. 8).

Another question is which a priori information to use for scattering related and other parameters. Very likely the future operational CarbonSat algorithm will use a priori

AMTD
6, 4769–4850, 2013

information for several parameters, as this will reduce systematic GHG retrieval errors. This is also the approach used by the operational GOSAT algorithm (Yoshida et al., 2011, 2013). Here we utilize the following simple approach: We use constant a priori values for COD, CTH and AOD but to compensate for this we assume good knowledge of the surface albedo by using the true albedo in each band as first guess value. Note that BESD/C retrieves surface albedo (see ALB state vector elements listed in Table 2) and first guess values are obtained using a pre-processing scheme based on transparent spectral regions as located in each of the three bands. Nevertheless, systematic XCO_2 and XCH_4 retrieval errors are reduced if surface albedo is well known, especially for low albedo scenes, where aerosols and cirrus may significantly influence the backscattered radiance.

4.2 Error analysis based on individual BESD/C retrieval

For the error analysis (and the error parameterization, see following section) a number of scenarios have been defined using different combinations of COD, CTH, AOD, surface albedo and SZA. They are shown in Fig. 5. For each scenario high spectral resolution radiance spectra have been computed with SCIATRAN and converted to simulated CarbonSat spectral observations using the CarbonSat instrument model mentioned in Sect. 2. BESD/C has been applied to each simulated observation to retrieve XCO_2 and XCH_4 and to determine their errors. Random errors depend primarily on the signal-to-noise performance of the instrument and the OE retrieval method permits one to map this error from radiance space to state vector (i.e. retrieval parameter) space. Systematic XCO_2 and XCH_4 errors are computed as "retrieved minus true", where the true values are the known values from the model atmosphere. After BESD/C retrieval, a quality flag is set, which depends on the retrieved scattering parameters. Here we only flag those retrievals as "good" for which the sum of the retrieved aerosol optical depth (at NIR wavelength) and cirrus optical depth is less than 0.3 (i.e. AOD(NIR) + COD < 0.3). This filtering criterium is similar as used, for example, for GOSAT XCO_2 retrieval (Guerlet et al., 2013b; O'Dell et al., 2012). Applying such

AMTD
6, 4769–4850, 2013

a criterium requires that COD and AOD (or strictly speaking their sum) can be retrieved with sufficient accuracy.

As shown in Fig. 5a, COD can be retrieved very well. This is shown by the typically very good agreement between retrieved COD (black dots) and true COD (green line). The retrieved AOD correlates with the true values but the absolute retrieved values are not perfect; typically the full variability is not captured by the retrieval. This shows that COD can be retrieved with higher accuracy than AOD. The reason for this is that the AOD changes are primarily due to changes of the aerosol amount in the boundary layer, which has less impact on the radiance than COD changes in the upper troposphere. As can also be seen in Fig. 5b, CTH can also be retrieved quite well at least if COD is not too low. Note that for this error analysis, as already explained, we only study very thin clouds as it is assumed that all ground pixels with significant cloud contamination have already been identified and removed (see also Sect. 5).

Figure 6 shows the corresponding XCO_2 and XCH_4 random and systematic errors for the same scenarios as shown in Fig. 5. The results for all scenarios are shown as light red line and the quality filtered, i.e. "good", retrievals are shown as red diamonds. Figure 7 is a zoom into Fig. 6 to show more details for all those scenarios, which correspond to a SZA of 50°.

As can be seen, the XCO_2 random error is typically around 1 ppm except for low surface albedo (see WAT50 scenarios in Figs. 6 and 7 corresponding to a water albedo of 0.03 in all spectral bands and a SZA of 50°), where the precision is close to 2 ppm, and for some high SZA scenarios (VEG75, i.e. vegetation albedo and SZA 75°, as shown in Fig. 6), where the XCO_2 precision exceeds 2 ppm for high COD. The XCH_4 random error has a similar scenario dependence. It is typically between 5–10 ppb except for the WAT50 and VEG75 scenarios, where it is typically between 15–20 ppb or even larger for VEG75, if COD is high.

The systematic errors are more complex as they depend more strongly on the scenario, especially for low albedo (WAT50) and high SZA (75°) scenarios (e.g. SAS75, corresponding to sand/soil albedo, and VEG75). For the "less extreme" albedo and

AMTD
6, 4769–4850, 2013

SZA scenarios (i.e. DES00, where DES is desert albedo, SAS25, VEG20, SAS50, and VEG50) the systematic XCO_2 error is a few tenths of a ppm and the systematic XCH_4 error is a few ppb. For the "more extreme" scenarios WAT50, SAS75 and VEG75, the systematic error can be much larger, up to about 3 ppm for XCO_2 and nearly 20 ppb for XCH_4. Also the dependence on cirrus OD, cirrus altitude and AOD is much larger for these scenarios. Because low albedos such as water (or snow and ice in the SWIR bands) result in large errors, we focus in this manuscript on (snow and ice free) land surfaces. It is believed that this will be much better when exploiting the CarbonSat sun-glint observations but a discussion of this is out of the scope of this study. The large variation of the errors at high SZA is also a potential problem. Therefore we limit the further analysis as presented in Sect. 5 and following sections to a maximum SZA of 70°.

4.3 Error parameterization

In order to generate one year of simulated CarbonSat observations we have developed an error parameterization scheme to parameterize the XCO_2 and XCH_4 random and systematic errors and their averaging kernels (which describe the change of the retrieved quantity, e.g. XCO_2, due to a change of the true quantity caused by a perturbation at a given altitude (e.g. the perturbation of the CO_2 mixing ratio). For this purpose we defined a number of regression functions and applied a linear regression scheme to the quality filtered, i.e. "good", retrievals, as shown in Figs. 6 and 7 (red diamonds) as already discussed in the previous section. The used error parameterization formulas and resulting regression coefficients are reported in Appendix A.

The error parameterization results for the XCO_2 and XCH_4 errors are shown in Figs. 6 and 7 (black dots). The error parameterization computes the desired output parameters based on 6 input parameters. The input parameters are the parameters which define the scenarios shown in Fig. 5, i.e. SZA, albedo in the NIR and SWIR-1 bands, COD, CTH and AOD (at 550 nm). These parameters are assumed to be the 6 most critical ones. Note that the errors also depend on other parameter not explicitely

AMTD
6, 4769–4850, 2013

considered here. One example is SWIR-2 albedo. SWIR-2 albedo variations have been considered for the retrieval simulations but not for the error parameterization. We assume here that the SWIR-1 and SWIR-2 albedos are sufficiently well correlated.

As can be seen from Figs. 6 and 7, the errors computed with the error parameterization method (black dots) capture the variability of the "real errors" (red diamonds) reasonably well. Less good is the agreement for very low surface albedos (WAT50 scenarios) and for scenarios where the SZA is large, i.e. the SAS75 and VEG75 scenarios. Figure 7, which is a zoom into Fig. 6, shows more details for the scenarios corresponding to a SZA of 50°. As can be seen most clearly in Fig. 6, the error parameterization tends to overestimate the random and systematic errors for typical land surfaces and tends to underestimate the errors for retrievals over water (i.e. for very low albedo scenes). As the focus of this manuscript is on observations over land, the error parameterization results are quite conservative as they tend to overestimate the random and systematic errors as computed using full BESD/C retrievals. In this context it shall be mentioned that also other error parameterization schemes have been investigated based on tabulating the errors obtained by BESD/C retrievals combined with a multi-dimensional interpolation scheme. The agreement of the results obtained with this scheme was however worse than for the scheme used here, especially for systematic errors, which exhibit complex dependencies on the various input parameters, and are therefore quite difficult to model. The main reason why the table-based interpolation scheme did not work well is because of problems related to the quality flagging, which essentially does not permit the generation of a table, which is based on a regular grid of input parameters.

The regression scheme also permits one to parameterize the XCO_2 and XCH_4 averaging kernels. The corresponding results are shown in Fig. 8. Shown are "real" (red diamonds) and parameterized (black dots) averaging kernel values at the surface (panels a and b) and at $p/p_s = 0.5$ (panels c and d), where p is the pressure level and p_s denotes surface pressure. As can be seen, the averaging kernels are nearly ideal, i.e. 1.0 at the surface for XCO_2 and XCH_4.

AMTD
6, 4769–4850, 2013

In the following section it is described how the error parameterization has been used to generate one year of simulated global CarbonSat observations.

5 Generation of simulated global CarbonSat observations

To generate a data set useful for global regional-scale inversion studies and other applications (see, e.g. Sect. 6) and to obtain statistical results for various regions (see Sect. 7), a one year global data set of simulated CarbonSat observations has been generated. This data set ("Level 2 error" – L2e – files) contains for each single CarbonSat observation the time and location of the measurement (for the reference year 2008), the relevant angles (e.g. solar and viewing zenith and azimuth angles) and various geophysical parameters such as AOD, COD and CTH. The files do not contain the XCO_2 and XCH_4 errors and the averaging kernels. Instead, these files contain all the needed information (for each ground pixel) to compute the corresponding values using the error parameterization method discussed in the previous section. The files also do not contain absolute XCO_2 and the XCH_4 values. These values are expected to come from a (global or regional) model as used for the analysis of the CarbonSat data. The model data are expected to be "perturbed", using the provided error characteristics (and averaging kernels) to generate appropriate simulated observations consistent with the model used.

The L2e files have been generated assuming an orbit similar as NASA's Terra satellite (sun-synchronous, descending, equator crossing 10.30 a.m., see www.nasa.gov/terra/) except for the equator crossing time, which is assumed to be 11.30 a.m. for CarbonSat, i.e. one hour later than Terra. One year of Terra data (year 2008) has been used to generate the L2e files. Geolocation information available in the Terra files has been used for the L2e files. The time information and related quantities, e.g. SZA, has been adjusted to consider the different equator overpass times.

The MODIS Terra MOD35 data product with a spatial resolution of about 1 km × 1 km has been used to identify and filter out cloud contaminated CarbonSat ground pixels.

AMTD
6, 4769–4850, 2013

Only those (2 km × 2 km) CarbonSat ground pixels are classified as cloud free for which all four corresponding MODIS pixels were cloud free. The L2e files only contain the cloud free CarbonSat data as determined using the described procedure. Nevertheless, it can be expected that some cloud contamination remains, in particular thin (sub-visual) cirrus clouds. In order to obtain the cirrus parameters COD and CTH, a "climatology" has been generated using CALIPSO (Winkler et al., 2009). The used CALIPSO data product (CAL LID L2 05kmCLay-Prov-V3-01) provides information on COD with a horizontal resolution of 5 km by 70 m. This data product has been processed as described in Heymann et al. (2012a). The CALIPSO data set provides binary information about cloud coverage. Consequently, the relative frequency of cloud occurrence has been computed for every grid box and is used as Cloud Fractional Coverage (CFC) data set. Using CALIPSO derived COD and CFC, "effective COD", eCOD (= COD × CFC), has been computed. The (sparse) CALIPSO eCOD and CTH data sets have been spatio-temporally smoothed with a Hann-window with an effective width of 8° × 8° and 3 months, i.e. the cirrus data sets used for this study are at much lower spatio-temporal resolution than the CarbonSat observations.

For aerosols the "GEMS aerosol product" (obtained from http://data-portal.ecmwf.int/data/d/gemsreanalysis/) as described and used in Heymann et al. (2012a), has been utilized. This data product is based on the assimilation of MODIS data. The time resolution is 12 hourly and the spatial grid is 1.125° × 1.125°. For this study primarily the AOD at 550 nm has been used.

For surface albedo, NASA's filled surface albedo data product has been used. This product is based on a climatology (2000–2004) of MODIS MOD43B3 data (http://modis-atmos.gsfc.nasa.gov/ALBEDO/index.html). This climatology removes snow-covered pixels, which is not a problem for this study, as we limit the analysis to snow and ice free land surfaces. For the NIR band we use the MODIS albedo at 860 nm.

A number of other parameters are also stored in the L2e files. One example is near surface wind speed (obtained from ECMWF meteorological data). This parameter is relevant, for example, for the analysis of sun-glint observations over water. It is however

AMTD
6, 4769–4850, 2013

not used for this study, which focuses on non-glint observations over land surfaces. Using these input parameters (all stored in the L2e files) and the error parameterization scheme, the XCO_2 and XCH_4 errors have been computed for each single CarbonSat ground pixel.

Figure 9 illustrates this by showing the greenhouse gas errors as computed using the error parameterization scheme described in Appendix A for a single CarbonSat overpass over Germany. Figure 10 shows several other parameters for the same overpass, which are used as input parameters for the error parameterization scheme: albedo, AOD, COD and CTH. The assumed swath width is 500 km (CarbonSat's goal swath width) corresponding to (at maximum, if all cloud free) 250 across-track ground pixels of size 2 km × 2 km. Gaps are due to thick clouds and additional quality filtering: Only those pixels are classified "good" for which the following conditions are all simultaneously met (simulated retrievals have shown that the quality of the retrievals is low if these conditions are not met):

- Cloud free (i.e. no thick clouds, see above),
- SZA $< 70^{\circ}$,
- Albedo(NIR) > 0.05,
- Albedo(SWIR-1) > 0.05,
- Albedo(NIR)/Albedo(SWIR-1) < 4, and
- AOD(550 nm) + COD < 0.4 (approximately equivalent to AOD(NIR) + COD < 0.3 (see Sect. 4) assuming a wavelength dependence of the aerosl extinction inversely proportional to wavelength).

As can be seen, the XCO_2 random error (i.e. the 1-sigma single measurement precision) is close to 1.2 ppm (Fig. 9a) with only some variations correlated with SWIR-1 albedo (Fig. 10a), as expected. This is also true for the XCH_4 random error (Fig. 9c), which is close to 7 ppb. The XCO_2 systematic error (Fig. 9b) typically differs from zero

AMTD
6, 4769–4850, 2013

and is about 0.3 ppm on average. Variations around the mean value of 0.3 ppm are in the range ±0.3 ppm also correlated with albedo (Fig. 10a), but likely also to some extent with AOD (Fig. 10c), COD (Fig. 10c) and CTH (Fig. 10d), although this is not so obvious, as these correlations are quite low. Note that the spatial fine structure of all errors is primarily due to surface albedo variations (in the NIR and SWIR bands) but not due to aerosols and cirrus, as these data sets were only available at quite low resolution (especially for cirrus) as already explained. This is assumed to be appropriate for regional-scale inversion studies (assuming that essentially only the "average error" matters) but not necessarily for "point sources" (see following section) such as power plants (e.g. Bovensmann et al., 2010; Krings et al., 2011) or cities (e.g. Kort et al., 2012; Schneising et al., 2013). This aspect is further discussed in the following section.

As can be seen from Fig. 9, the XCO_2 and XCH_4 errors are highly correlated, as both gases suffer from the same underlying error sources (either instrument noise or systematic scattering related errors). The results shown in Fig. 9 are based on BESD/C "Full Physics" (FP) retrievals. To a good approximation the data shown in Fig. 9 can be used to estimate the corresponding errors for "Proxy" (PR) retrievals. For PR retrieval, the "dry air column" needed to convert the vertical column of the target gas (as given in, for example, number of molecules per cm^2) to a column-averaged mole fraction or mixing ratio (ppm or ppb), is not obtained from surface pressure (and the retrieved water column) but using a reference gas with (approximately) known mixing ratio, here either CO_2 or CH_4, as already explained above. PR retrievals do not require the use of the O_2–A (i.e. NIR) band of CarbonSat. PR retrievals are therefore essentially based on the retrieved column ratio of the two gases (times a correction factor). In order to estimated PR retrieval errors using given FP retrieval errors, the following approach can be used:

The ratio of XCH_4/XCO_2 defines a conversion factor C between these two quantities, e.g. $C = 4.34$ ppb/ppm (= 1694.0 ppb/390.0 ppm) for the model atmosphere used here. Using this conversion factor, the XCO_2 random error for a PR retrieval is given by $\sqrt{\sigma^2_{CO_2,FP} + (\sigma_{CH_4,FP}/C)^2}$, where $\sigma_{CO_2,FP}$ is the XCO_2 FP random error and $\sigma_{CH_4,FP}$

AMTD
6, 4769–4850, 2013

is the $X\mathrm{CH_4}$ FP random error. The corresponding formula for the $X\mathrm{CH_4}$ PR random error is $\sqrt{\sigma^2_{\mathrm{CH_4,FP}} + (\sigma_{\mathrm{CO_2,FP}} \times C)^2}$. The $X\mathrm{CO_2}$ PR systematic error can be estimated via $\epsilon_{\mathrm{CO_2,FP}} - \epsilon_{\mathrm{CH_4,FP}}/C$, where the ϵ are the corresponding FP systematic errors. As can be seen from this formula, the $X\mathrm{CO_2}$ PR error would be zero if the two systematic errors (after conversion of $X\mathrm{CH_4}$ FP error to the corresponding $X\mathrm{CO_2}$ error) are identical. For example, if the $X\mathrm{CO_2}$ FP error is +1 % (+3.9 ppm) and the $X\mathrm{CH_4}$ FP error is also +1 % (+16.94 ppb corresponding to +3.9 ppm after conversion), the $X\mathrm{CO_2}$ PR error would be zero. If however, in this case, the $X\mathrm{CH_4}$ error would be −1 % instead of +1 %, the two errors would not cancel but add to a +2 % (+7.8 ppm) $X\mathrm{CO_2}$ PR error. The $X\mathrm{CH_4}$ PR systematic error can be estimated using an analoge formula via $\epsilon_{\mathrm{CH_4,FP}} - \epsilon_{\mathrm{CO_2,FP}} \times C$.

Figure 11 illustrates this. The "PR errors" shown Fig. 11 are the "FP errors" shown in Fig. 9 but converted to PR errors using the formulas given here. As can be seen, the PR random errors are larger than the FP errors, but the systematic PR errors are much smaller compared to the corresponding FP errors due to cancellation of errors, as expected. For the systematic $X\mathrm{CO_2}$ errors the variation over the scene is only about 0.2 ppm, i.e. about a factor of four smaller compared to the FP errors. For $X\mathrm{CH_4}$ the results are similar; the systematic $X\mathrm{CH_4}$ PR error varies only about 1 ppb over the scene, which is also about four times smaller compared to the FP error. For random errors the opposite is true: the PR random errors are about 83 % larger for $X\mathrm{CO_2}$ (2.2 ppm instead of typically 1.2 ppm for FP retrievals) and about 28 % larger for $X\mathrm{CH_4}$ (9 ppb instead of typically 7 ppb).

In the following section, the data set shown in Fig. 9 is further discussed by using it to investigate to what extent CarbonSat can contribute to quantify anthropogenic $\mathrm{CO_2}$ emissions of large cities using Berlin, the capital of Germany, as an example.

AMTD
6, 4769–4850, 2013

6 First application: Berlin CO_2 emissions from single "XCO_2 images"

In this section the data set presented in the previous section is used to investigate how accurately and precisely the anthropogenic CO_2 emissions of large cities can be derived from single overpass CarbonSat XCO_2 data, i.e. from so-called "XCO_2 images" as shown in, for example, Fig. 9.

Cities and large urban areas are home to the majority of today's world population and are responsible for more than two thirds of the global energy-related CO_2 emissions. As pointed out in NRC (2010), and Kort et al. (2012) many cities have emission reduction policies in place, but lack objective, observation-based methods for verifying their outcomes. In a recent study, McKain et al. (2012), argue that observations of column-averaged carbon dioxide, e.g. from space, are presumably the most suitable method to detect emissions and emission trends from urban regions.

However, none of the existing satellites has been designed for such an application. Nevertheless, first attempts have been made to detect and quantify anthropogenic urban area CO_2 emissions using existing space-based observations. Schneising et al. (2008), analyzed three years of SCIAMACHY XCO_2 retrievals and showed that regionally elevated CO_2 over the highly populated region of western central Germany and parts of the Netherlands ("Rhine-Main area") correlate with anthropogenic CO_2 emissions. In a follow-on study, Schneising et al. (2013), extended this analysis by also studying other regions and using a longer SCIAMACHY time series. They found, for example, for the highly populated Yangtze River Delta in China that a distinct positive trend of the regional XCO_2 enhancement exists, which is quantitatively consistent with anthropogenic emissions in terms of relative increase per year. Other studies focused on individual cities, primarily megacities such as Los Angeles (Wunch et al., 2009). Kort et al. (2012), found that by differencing GOSAT observations over megacities with those in nearby background, robust, statistically significant XCO_2 enhancements of 3.2 ± 1.5 ppm for Los Angeles and 2.4 ± 1.2 ppm for Mumbai can be derived. They conclude that these enhancements can be exploited to track anthropogenic emission

AMTD
6, 4769–4850, 2013

trends over time. Keppel-Aleks et al. (2012), studied to what extent space-based observations of XCO_2 help to constrain fossil fuel CO_2 emissions by using model simulations and GOSAT XCO_2 retrievals. They discuss how their approach can be used as a policy tool to verify national fossil emissions, as it provides an independent, observational constraint. They conclude that their model simulations clearly show the potential of their proposed approach but that their analysis using real GOSAT data is limited by the sparseness of the GOSAT data.

CarbonSat will deliver several orders of magnitude more data than GOSAT. One GOSAT observation requires 4 s but CarbonSat will deliver several hundred observations each second. In the following we present a first analysis aiming to answer the question of how accurately, precisely and frequently CarbonSat will be able to deliver information on city CO_2 emissions. For this purpose we show first results for Berlin. Berlin is a typical large city but not a megacity. Therefore Berlin has been selected but also because it is the capital of Germany, the home country of most of the authors of this study. Berlin is located in the north-east of Germany, covers a size of approximately 892 km^2, and has about 3.5 million inhabitants. Berlin is relatively well isolated, i.e. not a part of a large agglomeration of several cities. This is an advantage for the purpose of this study as it permits to clearly identify the anthropogenic CO_2 emission plume of Berlin in single CarbonSat "XCO_2 images".

For this study we used a relatively high-resolution CO_2 modeling system and resulting data set for Europe as described in Pillai et al. (2010). The modeling system is based on the (Eulerian) high-resolution transport model WRF (Weather Research and Forecasting) coupled to a diagnostic vegetation model, the Vegetation Photosynthesis and Respiration Model (VPRM), to obtain a realistic distribution of atmospheric CO_2. The model set up utilizes high-resolution fossil fuel emission data at a spatial resolution of 10 km, prescribed from IER (Institut für Energiewirtschaft und Rationelle Energieanwendung), University of Stuttgart, Germany (http://carboeurope.ier.uni-stuttgart.de) to account for anthropogenic fluxes. Initial and lateral CO_2 tracer boundary conditions are calculated by the global atmospheric tracer transport model, TM3 (Heimann et al.,

AMTD
6, 4769–4850, 2013

2003), operated by MPI-Biogeochemistry (MPI-BGC) in Jena. These simulations are utilized to infer the Berlin emissions using a simple inverse modelling scheme based on linear least-squares with two free parameters: a constant offset for the entire analysed scene and a scaling factor for the anthropogenic XCO_2 spatial pattern. We consider systematic errors of the CarbonSat XCO_2 retrievals and also quantify the systematic error of the inferred emission caused by biogenic XCO_2 variations. This is considered appropriate for the purpose of this study, which focuses on CarbonSat related errors, especially on estimating how random and systematic XCO_2 errors map onto emission errors. For the future it is planned to use a more sophisticated inverse modelling method, for example, based on STILT (the Stochastic Time-Inverted Lagrangian Transport model) following the method described in Pillai (2011), using the inversion scheme of Gerbig et al. (2003) and Lin et al. (2004). STILT can be used as an adjoint of the Eulerian modelling system WRF-VPRM to derive biosphere-atmosphere exchange on local to regional scales (depending on the information content of the observations) from measured CO_2 mixing ratios (Pillai et al., 2012).

For this study we use WRF-VPRM simulations at 10 km × 10 km hourly resolution for three days mainly analyzing the data around local noon. These three days, in the following referred to as "scenarios" S1, S2, and S3, are described in Table 3. Scenarios S1 and S2 correspond to typical weekdays, where the anthropogenic (fossil) CO_2 emission of Berlin is assumed to be approximately 54 $MtCO_2\,yr^{-1}$ (according to IER). The XCO_2 enhancement of the CO_2 emission plume of Berlin relative to the background XCO_2 is 1.47 ppm (at 10 km × 10 km resolution) for S1, where the near-surface wind speed is around 4.5 $m\,s^{-1}$ (Table 3). As expected (see, e.g. Bovensmann et al., 2010), the amplitude of the emission plume is approximately inversely proportional to near-surface wind speed. Therefore, for scenario S2, where the wind speed is 7.4 $m\,s^{-1}$, the XCO_2 enhancement is reduced to 0.88 ppm. Scenario S3 corresponds to a Sunday. During Sundays the emissions are typically much lower than during weekdays, namely 31 $MtCO_2\,yr^{-1}$ for S3 (according to IER for the day studied). The wind speed for S3 is 5.1 $m\,s^{-1}$ and the XCO_2 enhancement due to the Berlin emissions is 0.54 ppm.

AMTD
6, 4769–4850, 2013

Figure 12 shows the XCO_2 contribution at 10 km × 10 km resolution of the biogenic fluxes (computed via VPRM, see above), the anthropogenic CO_2 emissions (using IER) and the corresponding anthropogenic XCO_2 contribution to the total XCO_2 for the three scenarios S1, S2 and S3 as computed with the WRF-VPRM modelling system. Berlin is located in the centre of the region shown in Fig. 12. Also shown (as a white rectangle) is the "target region" used for inferring the Berlin anthropogenic CO_2 emissions from the CarbonSat observation. The centre of the target region is Berlin (latitude 52.5° N, longitude 13.4° E) and the spatial extent is 3° × 3°.

As can be seen from Fig. 12, the modeled biogenic component of the XCO_2 is negative because in summer atmospheric CO_2 is taken up by growing vegetation resulting in a CO_2 flux from the atmosphere to the surface. More important for the purpose of this study is the spatial variation of the "disturbing" biogenic XCO_2 in the target region. As can be seen, the biogenic XCO_2 varies over the target region by about 0.5–2 ppm depending on scenario. Most critical for the purpose of this study are correlations of the biogenic XCO_2 pattern (Fig. 12, left panels) with the anthropogenic XCO_2 pattern (Fig. 12, right panels). The lower the correlations, the better the two components can be disentangled and the lower the systematic error of the CarbonSat-inferred anthropogenic CO_2 emissions. Note that the distance of the target centre to one of its boundaries, which is 1.5°, roughly corresponds to 150 km, which corresponds to approx. 8 h for air parcels travelling with 5 m s^{-1}. This means that the CO_2 emission plume is not only determined by the emission at the time of the overpass but by the (time dependence of) the emission during a time interval of several hours before the time of the overpass. This is considered when modelling the CO_2 emission plume. For the inversion results shown here it is assumed that the time dependence of the emissions in the time period of up to several hours before the overpass is sufficiently well known.

In the following we focus on investigating the impact of various systematic errors on the derived Berlin emissions. However, also the statistical (random) error of the derived emission is presented and discussed. It originates primarily from the random error of the measured XCO_2 which in turn is primarily due to instrument (detector) noise (but

AMTD
6, 4769–4850, 2013

which also to some extent depends on the retrieval algorithm). The XCO_2 random error is shown in Fig. 13, which is essentially a zoom into the data shown in Fig. 9a.

Systematic CarbonSat XCO_2 errors for scenario S1 are shown in Fig. 14 (left row). The top left panel is essentially a zoom into Fig. 9b, i.e. the error is the error as computed via the error parameterization using the smooth aerosol input data as shown in Fig. 10b. The top right panel shows the "observed XCO_2" in the Berlin centered target region, computed using the modeled XCO_2 plus the systematic error as shown in the top left panel. Here the modeled XCO_2 is the anthropogenic XCO_2 component only (model "A"), see middle right panel of Fig. 12. An offset (0.22 ppm, see figure annotation) has been subtracted. Here it is essentially assumed that the XCO_2 variability in the target region is dominated by anthropogenic CO_2 emissions and that, for example, XCO_2 from biogenic fluxes is essentially constant over the target region or that this component can be subtracted from the observations (we also investigate what happens if this assumption is not valid, see below). The Berlin assumed anthropogenic CO_2 emission is 54.80 $MtCO_2\,yr^{-1}$ (see annotation).

Two additional numbers are listed in Fig. 14, which have been computed using the CO_2 emission inversion scheme: the random error (RE, in red) of the Berlin CO_2 emission as obtained by inverting the CarbonSat observations and the systematic error (SE, in black). These numbers have been obtained via the simple inversion scheme explained above. The basic assumption is that the spatial XCO_2 pattern can be modelled sufficiently well, not however its amplitude, which depends on the unknown anthropogenic CO_2 emission of Berlin. As explained, the inversion model has two free parameters: an offset and a second parameter, which scales the modeled anthropogenic XCO_2 spatial pattern. The offset considers the variable and not well known CO_2 background concentration. If the observed XCO_2 (Fig. 14, top right panel) differs from the modeled anthropogenic XCO_2 pattern, the retrieved CO_2 emission will typically differ from the true emission. In this case a systematic error of the retrieved CO_2 emission results. The size of this error depends on how much the XCO_2 systematic error correlates with the modeled XCO_2 pattern as used by the least squares procedure. Here the

AMTD
6, 4769–4850, 2013

systematic error (SE) is +0.66 $MtCO_2\,yr^{-1}$ (+1.2 %) as shown in the figure annotation. It originates from the fact that the CarbonSat XCO_2 systematic error to some extent correlates with the Berlin CO_2 emission plume. The random error (RE) of the inferred emission is 4.53 $MtCO_2\,yr^{-1}$ (8.3 %). It originates from the XCO_2 random error shown in Fig. 13.

These results have been obtained using the systematic error computed using the (quite low resolution) AOD data shown in Fig. 10b. This systematic CarbonSat XCO_2 error is in the following referred to as "H0". These AOD data are assumed to be be appropriate for large-scale inversion studies (as explained above) but not necessarily for point sources and cities. The reason is that one would expect that the Berlin pollution plume contains not only additional CO_2 (relative to the background) but also additional aerosols. Therefore the potential impact of high spatial resolution aerosol variations has also been studied. A similar assessment has been made in Bovensmann et al. (2010) and Krings et al. (2011). To convert a local XCO_2 enhancement to a local AOD enhancement (at 550 nm), Bovensmann et al. (2010) used an AOD enhancement of 0.5 per 1 % (4 ppm) XCO_2 enhancement. Krings et al. (2011), argue that this estimate is much too conservative and use an AOD enhancement of 0.05 per 1 % XCO_2 enhancement. For this study we use a value in between, namely ΔAOD(550 nm) = 0.2 per 4 ppm ΔXCO_2, i.e. anthropogenic XCO_2 enhancement. We have used the error parameterization formula (Appendix A) to compute the derivative of the XCO_2 systematic error due to an AOD enhancement, ΔAOD, for each single CarbonSat observation shown in Fig. 9 and have multiplied these values with the modeled anthropogenic XCO_2 plume to get a likely more realistic XCO_2 systematic error ("H1"; Fig. 15 shows the difference between the systematic errors H1 and H0). Note that we consider the worst case situation as it is assumed here that the aerosol error is perfectly correlated with the Berlin CO_2 plume. The results are shown in the middle row of Fig. 14. As can be seen, the systematic error of the inferred CO_2 emission of Berlin is 4.98 $MtCO_2\,yr^{-1}$ (9.1 %), i.e. significantly larger than for error H0 assumed for the results shown in the top row.

AMTD
6, 4769–4850, 2013

So far we have assumed that the spatial XCO_2 variability in the target region is only due to anthropogenic CO_2 (which is not true, see Fig. 12, left panels) or that other contributions, most notably biogenic XCO_2, can be accurately modeled (at least apart from a constant scaling factor for the spatial pattern of the biogenic XCO_2, which could be added as an additional parameter in the inversion scheme; this however has not been done for the results shown here). For the results shown in the bottom row of Fig. 14 we assume the other extreme, namely that the biogenic XCO_2 is a perturbation that cannot be modeled at all and therefore is not considered in the least squares inversion model but is present in the observed XCO_2 (see Fig. 14, bottom right), which is modeled using "model AB", which computes XCO_2 as the sum of the anthropogenic and the biogenic XCO_2. As can be seen, the systematic error of the Berlin emission is $8.83\,MtCO_2\,yr^{-1}$ (16.1 %) in this case. Note that here we also use the worst case assumption of additional aerosols perfectly correlated with the Berlin CO_2 emission plume (i.e. systematic XCO_2 error "H1") as also used for the results shown in the middle row. The results shown in the bottom row of Fig. 14 are therefore a worst-case estimate of the systematic error of the inferred CO_2 emission of Berlin for a single CarbonSat Berlin overpass.

We have performed the same investigation for the scenarios S2 (Fig. 16) and S3 (Fig. 17). The results for all three scenarios are summarized in Table 4. Comparing the random errors (precision) listed in Table 4 with the near-surface wind speeds for S1, S2 and S3 listed in Table 3, one finds that the random errors is proportional to wind speed and that, consistent with the results shown in Bovensmann et al. (2010), the random emission error is approximately $1\,MtCO_2\,yr^{-1}$ per $1\,m\,s^{-1}$ wind speed (i.e. approximately $5\,MtCO_2\,yr^{-1}$ for $5\,m\,s^{-1}$, etc.). For the real CarbonSat data the systematic emission error will likely be in between the quite extreme cases studied here. Note that the assumption used for "model A", namely that only the anthropogenic XCO_2 pattern is relevant, can be tested using real CarbonSat data (when available) by subtracting the modeled biogenic XCO_2 from the Carbonsat observations and investigating if the

AMTD
6, 4769–4850, 2013

remaining XCO_2 pattern is consistent with the expected CO_2 anthropogenic city emission plume or not.

We have analyzed the entire one year data set of CarbonSat observations using the 9 cases listed in Table 5. For case S1_H1_A, i.e. using scenario S1, systematic error H1, and model A, detailed results are shown in Fig. 18. Shown are the random and systematic CO_2 emission errors for all days where a "good" overpass occurred (defined by a sufficiently large number of observations at and around Berlin). The results are shown for a swath width of 240 km (black) and 500 km (green). The number of good overpasses is 22 for a swath width of 240 km and 39 for a swath width of 500 km. Also listed are a number of statistical figures of merit characterizing the random and systematic errors for both swath widths. The analysis as presented in Fig. 18 has been conducted for all 9 cases and the results are summarized in Table 5.

It has to be pointed out that the model simulations used here are at 10 km × 10 km resolution, which is coarser that the CarbonSat resolution of 2 km × 2 km. Efforts are underway to fully exploit the high resolution observations of CarbonSat by using a higher resolution modeling and inversion system. It can be expected that using higher resolution (inverse) modeling, systematic error can be reduced by better disentangling biogenic XCO_2 variations from anthropogenic XCO_2 signals but to what extent this is possible needs to be quantified in a future study.

Overall it can be concluded from the results shown here that by using CarbonSat single overpass XCO_2 one can detect and quantify the anthropogenic CO_2 emissions of cities such as Berlin. The single observation random error is approximately 5–10 $MtCO_2\,yr^{-1}$ (10–20 % for Berlin). Systematic errors are expected to be on the same order. Their magnitude depends on which assumptions are used for the observational and modeling errors.

AMTD
6, 4769–4850, 2013

7 Analysis of global data

The CarbonSat observations will also be used to quantify CO_2 and CH_4 fluxes globally at regional scale spatial resolution and approximately monthly time resolution. In this section we present an overview about the global data. We discuss spatio-temporal averages of the XCO_2 and XCH_4 random and systematic errors, obtained from averaging the data contained in the L2e files, and also present detailed results for selected regions.

Figure 19 shows spatio-temporally averaged errors for July for a spatial grid of $5^\circ \times 5^\circ$. As can be seen, the mean XCO_2 random error (panel a) is typically close to 1.1 ppm, except for highly reflecting surfaces such as the Sahara, where the mean precision is in the range 0.5–0.8 ppm (simple direct average, i.e. not divided by the square root of the number of observations or equivalent). The mean systematic XCO_2 error (panel b) is typically within ±0.3 ppm but may reach or even exceed 0.4 ppm (positive and negative biases). The mean XCH_4 random error (panel c) is typically close to 7 ppb, except for highly reflecting surfaces such as the Sahara, where the mean precision is as low as approximately 4 ppb. The mean systematic XCH_4 error (panel d) is typically within ±2 ppb but also reaches approximately −4 ppb over large parts of central Africa. The number of observations is very large as shown in Fig. 20. Depending on the month, the number of quality filtered observations over snow and ice free land surfaces is in the range of 33–46 million per month. As described, the random and systematic errors are caused by and depend on critical parameters which have been used as input for the error parameterization scheme. For comparison with Fig. 19, these input parameters are shown in Fig. 21.

Finally, we present detailed results for selected regions, which are listed in Table 6. For each of these regions cumulative error distributions have been computed as shown in Figs. 22 and 23 and summarized in Table 6. As can be seen, systematic errors are mostly (approx. 85 %) below 0.3 ppm for XCO_2 (< 0.5 ppm: 99.5 %) and below 2 ppb for XCH_4 (< 4 ppb: 99.3 %). This finding together with the high single measurement

AMTD
6, 4769–4850, 2013

precision and the large amounts of data to be expected from CarbonSat indicates that CarbonSat will be able to make significant contributions for improving our knowledge on the sources and sinks of these two very important greenhouse gases.

8 Limitations and outlook to future work

The error parameterization scheme permits one to compute random and systematic scattering related XCO_2 and XCH_4 errors for the six input parameters solar zenith angle, surface albedo in two bands, aerosol and cirrus optical depth, and cirrus altitude. As already pointed out, this scheme is more complex that previously used error parameterization schemes developed for other satellite missions (e.g. Hungershoefer et al., 2010) but it is still quite simple. For example, aerosol type variations are neglected and it is assumed that aerosol variability is confined to the boundary layer (here the lowest 2 km of the atmosphere).

For the error parameterization the aerosol type "Continental Average" (CA) from OPAC (Hess et al., 1998) is used as implemented in the radiative transfer model SCIATRAN (Rozanov and Kokhanovsky, 2006; Kauss, 1998). This aerosol type consists of a mixture of three components: "soot" (fraction: 0.541987), "water-soluble" (0.457987), and "dust-like" (0.000026). While this is assumed to be a reasonable choice for "average conditions" for observations over land, this does not cover, for example, more polluted scenes. To estimate the impact of this assumption we have performed a limited number of simulated retrievals. For example, when applying the BESD/C retrieval algorithm to a combination of different AODs, CODs and CTHs (45 combinations) we found for the VEG50 scenario (i.e. vegetation albedo and SZA 50°) that the mean XCO_2 bias and its scatter (1 sigma) is -0.18 ± 0.27 ppm for CA aerosol (XCH_4: -1.11 ± 1.83 ppb). When generating the simulated CarbonSat observations assuming that the aerosol is OPAC "Continental Polluted" (CP), the biases are very similar as for CA aerosols: -0.14 ± 0.31 ppm for XCO_2 and -1.09 ± 1.69 ppb for XCH_4 (for the CP aerosol the errors are even somewhat smaller but note that this is not a comparison between identical

AMTD
6, 4769–4850, 2013

scenes because of the quality filtering). The main difference between the two aerosol types are: CP aerosols contain more "soot" (69 % compared to 54 % for CA) but less "water-soluble" aerosol (31 % compared to 46 % for CA). However, aerosols are highly variable and errors can be larger depending on aerosol type. For example aerosol type "Desert", which consists of much larger particles than CA and CP aerosols (composition: 87.1 % "water soluble" 11.7 % "mineral/nuclei mode", 1.1 % "mineral/accumulation mode"), the biases are 0.54 ± 0.40 ppm for XCO_2 and 2.63 ± 2.10 ppb for XCH_4 as determined using the version of the BESD/C algorithm and its parameter settings including filtering criteria as used in this publication. Here a clear tendency for a high bias can be observed. This is partly because of a high bias (outlieres) for certain scenes which are not filtered out (i.e. detected) by the currently used quality filtering scheme. Larger errors may also occure if the aerosol profile variability is not dominated by variability in the boundary layer (here: 0–2 km) but by variations in higher altitudes. For example, if we generate simulated CarbonSat observation with CP aerosols using extinction profiles which peak in the 2–4 km region the biases are 0.41 ± 0.71 ppm for XCO_2 and 1.96 ± 3.16 ppb for XCH_4 (for the retrieval we assume, as usual, CA aerosols mainly in the 0–2 km region). This shows that aerosol (and cirrus) type and vertical profile variations cannot be neglected. To better address these aspects will be a focus of our future activities.

We also plan to improve the analysis of how accurately, precisely and frequently anthropogenic CO_2 emissions of large cities such as Berlin can be derived from CarbonSat observations. This will include the study of other cities but also a refinement of the initial results presented here for Berlin. The latter will comprise detailed modelling of the anthropogenic and biogenic XCO_2 pattern for each single overpass instead of analyzing a limited number of scenarios as done here. It is expected that this will result in a somewhat reduced number of "good overpasses" as estimated here due to the possible inclusion of less favorable conditions (e.g. wind directions which do not permit one to clearly separate the Berlin emission plume from non-Berlin anthropogenic XCO_2 contributions).

AMTD
6, 4769–4850, 2013

9 Conclusions

The objective of the CarbonSat mission is to improve our understanding of natural and anthropogenic sources and sinks of the two most important anthropogenic greenhouse gases (GHG) carbon dioxide (CO_2) and methane (CH_4). The unique feature of CarbonSat is its "GHG imaging capability", which is achieved via a combination of high spatial resolution (2 km × 2 km) and good spatial coverage achieved by a relatively wide swath and no gaps between ground pixel. The width of the across-track swath has not yet been finally decided. Here we presented results for two swath widths: 240 km (CarbonSat's breakthrough requirement) and 500 km (goal requirement). This capability enables global imaging of localized strong emission sources such as cities, power plants, methane seeps, landfills and volcanos and better disentangling of natural and anthropogenic GHG sources and sinks.

Source/sink information can be derived from the retrieved atmospheric column-averaged mole fractions XCO_2 and XCH_4 (Level 2 products) via inverse modeling. We have presented an error analysis for CarbonSat XCO_2 and XCH_4 retrievals focusing on scattering related errors due to clouds and aerosols. The results have been obtained using the BESD/C "full physics" (FP) retrieval algorithm and using the most recent instrument and mission specification.

Errors due to aerosols and thin cirrus clouds are expected to dominate the error budget especially for XCO_2 systematic errors. In order to quantify random and systematic errors, a one year data set of simulated CarbonSat nadir mode observations over land has been generated and analyzed. This has been achieved by developing an error parameterization scheme, which permits fast computation of random and systematic XCO_2 and XCH_4 retrieval errors and averaging kernels. The method is based on applying the BESD/C FP algorithm to simulated CarbonSat observations. The resulting XCO_2 and XCH_4 errors and averaging kernels have been parameterized using a linear regression method.

AMTD
6, 4769–4850, 2013

We have focused on scattering related errors obtained with the BESD/C FP retrieval method and using an error parameterization scheme which permits one to compute random and systematic errors for one year of simulated CarbonSat observations. Using this method, we have shown that systematic errors are mostly (approx. 85 %) below 0.3 ppm for XCO_2 (< 0.5 ppm: 99.5 %) and below 2 ppb for XCH_4 (< 4 ppb: 99.3 %). The single measurement precision is typically 1.2 ppm for XCO_2 and 7 ppb for XCH_4 (1-sigma). For "proxy" (PR) retrievals, which are based on the retrieved CH_4 to CO_2 column ratio (or its inverse, depending on application), it has been estimated that the systematic errors are about a factor of four smaller compared to FP retrievals but that the PR random errors are about 83 % larger for XCO_2 (2.2 ppm instead of typically 1.2 ppm for FP retrievals) and about 28 % larger for XCH_4 (9 ppb instead of typically 7 ppb). We also have shown that the number of quality filtered observations per month over cloud and ice free land surfaces is in the range 33–46 million per month depending on month.

CarbonSat will also provide valuable information on Vegetation Chlorophyll Fluorescence (VCF) retrieved from clear Fraunhofer lines located around 755 nm. We estimate that the VCF single measurement precision is approximately 0.3 $mW\,m^{-2}\,nm^{-1}\,sr^{-1}$ (1-sigma) at 755 nm. For GOSAT, Frankenberg et al. (2012) found that the achieved single measurement precision is 0.5 $mW\,m^{-2}\,nm^{-1}\,sr^{-1}$ (1-sigma) at 755 nm. According to Guanter et al. (2010), VCF retrieval errors less than about 0.5 $mW\,m^{-2}\,nm^{-1}\,sr^{-1}$ would be valuable measurements as, for example, the expected signal variation at 760 nm is assumed to be in the range 0–4 $mW\,m^{-2}\,nm^{-1}\,sr^{-1}$.

Systematic VCF errors as determined using the very fast but simple retrieval method presented here are typically less than 0.2 $mW\,m^{-2}\,nm^{-1}\,sr^{-1}$. This systematic error estimate however does not include potential other error contributions such as intensity offsets (due to imperfect calibration). It also does not include possible errors due to Rotational Raman Scattering (RRS), which are expected to be small but may not be entirely negligible (Vasilkov et al., 2013).

AMTD
6, 4769–4850, 2013

As a first application the data set has been used to assess the capability of CarbonSat to quantify the CO_2 emissions of large cities using Berlin, the capital of Germany, as an example. It has been shown that the precision of the inferred Berlin CO_2 emissions obtained from single CarbonSat overpasses is in the range 5–10 $MtCO_2\,yr^{-1}$ (10–20 %). Systematic errors could be on the same order. Our estimates depend on which assumptions are used with respect to observational systematic errors and biogenic XCO_2 modeling errors.

The results presented here indicate that CarbonSat will be able to make significant contributions to improving our knowledge on the sources and sinks of these two very important greenhouse gases. The data set presented here is currently being evaluated using global regional-scale inverse modeling to quantify this statement.

Finally, we have pointed out some of the limitations of the error parameterization method. Our scheme is more complex than previously used error parameterization schemes developed for other satellite missions (e.g. Hungershoefer et al., 2010) but it is still quite simple. For example, aerosol type variations are neglected and it is assumed that aerosol variability is confined to the boundary layer. To better address these aspects will be a focus of our future activities.

Appendix A

Error parameterization

Linear regression has been used to parameterize the XCO_2 and XCH_4 random and systematic errors (four quantities) and their averaging kernels. The averaging kernels (AK) as a function of pressure level (p, used as vertical coordinate), AK(p), are approximated by a low-order polynomial defined by the three polynomial coefficients P0, P1, P2, such that $AK(p) = P0 + P1*p/p_\circ + P2*(p/p_\circ)^2$, where $p_\circ$ is surface pressure. Three coefficients are used for the XCO_2 AK and three for the XCH_4 AK. In total 10 quantities have been parameterized.

AMTD
6, 4769–4850, 2013

The regression function used for the parameterization of each parameterized quantity Q is:

$$Q = \sum_{i=0}^{7} C_i X_i. \quad \text{(A1)}$$

Here Q is any of the 10 to-be-parameterized quantities and X_i is the i-th regression function and C_i the corresponding regression coefficient. The regression functions are identical for all 10 quantities but the regression coefficients differ for each quantity. The regression functions are listed in Table 7 and the corresponding coefficients in Table 8. Regression function X_0 is a constant (offset). Each of the regression functions X_1-X_7 correspond to one of the six key inputs parameters (e.g. SZA, NIR albedo) or a combination of them (X_7) as listed in Table 7. Table 7 also lists the valid range of these input parameters (for example, the regression should not be used for SZA larger than about 80°).

After computation of Q according to Eq. (A1), some further computations are needed to compute the final values of the XCO_2 and XCH_4 random and systematic errors: random errors: if the XCO_2 or XCH_4 random errors are less than (the pre-defined minimum value of) 0.7 ppm for XCO_2 and 4.2 ppb for XCH_4, the corresponding values should be set to these minimum values. This avoids unrealistically small (or even negative) random errors. Systematic errors: For the XCO_2 and XCH_4 systematic errors a "SZA bias correction" should be applied as follows: For XCO_2 the term SZA/70-0.2 should be subtracted, and for XCH_4 the term 8.0 × SZA/70.0-1.0. Without this correction the global bias maps (e.g. Fig. 9b and d) would show an obvious SZA dependent bias at high SZA, which could very likely be identified and corrected for when analyzing real CarbonSat data. More advanced bias correction schemes such as the ones currently used for, e.g. real GOSAT data (e.g. Crisp et al., 2012; Cogan et al., 2012), are however not used in this study.

AMTD
6, 4769–4850, 2013

Acknowledgements. We thank the NASA Langley Research Center Atmospheric Science Data Center for providing us with the CALIOP/CALIPSO data. We also thank NASA for the various MODIS data products used for our research (e.g. the MODIS/Terra products obtained from www.nasa.gov/terra/ and the NASA's filled surface albedo product based on MODIS MOD43B3 obtained from http://modis-atmos.gsfc.nasa.gov/ALBEDO/index.html). We thank ECMWF for providing meteorological data. We also thank ECMWF and the European GEMS/MACC-II project for the global aerosol data set (obtained from http://data-portal.ecmwf.int/data/d/gems/reanalysis/) also based on MODIS data. We also thank Julia Marshall, MPI-BGC, Jena, Germany, for helpful comments. This study has been funded by ESA (project "CarbonSat Earth Explorer 8 Candidate Mission, Level-2 and Level-lB requirements consolidation" (led by IUP, Univ. Bremen, via ESA Contract No 4000105676/12/NL/AF) and project "LOGOFLUX – CarbonSat Earth Explorer 8 Candidate Mission – Inverse Modelling and Mission Performance Study" (led by NOVELTIS, Toulouse, France, via ESA Contract No 400010537/12/NL/CO) and by the University and the State of Bremen.

References

Basu, S., Guerlet, S., Butz, A., Houweling, S., Hasekamp, O., Aben, I., Krummel, P., Steele, P., Langenfelds, R., Torn, M., Biraud, S., Stephens, B., Andrews, A., and Worthy, D.: Global CO_2 fluxes estimated from GOSAT retrievals of total column CO_2, Atmos. Chem. Phys. Discuss., 13, 4535–4600, doi:10.5194/acpd-13-4535-2013, 2013. 4772

Bergamaschi, P., Frankenberg, C., Meirink, J. F., Krol, M., Villani, M. G., Houweling, S., Dentener, F., Dlugokencky, E. J., Miller, J. B., Gatti, L. V. Engel, A., and Levin, I.: Inverse modeling of global and regional CH_4 emissions using SCIAMACHY satellite retrievals, J. Geophys. Res., 114, D22301, doi:10.1029/2009JD012287, 2009. 4772

Boesch, H., Baker, D., Connor, B., Crisp, D., and Miller, C.: Global characterization of CO_2 column retrievals from shortwave-infrared satellite observations of the orbiting carbon observatory-2 mission, Remote Sens., 3, 270–304, doi:10.3390/rs3020270, 2011. 4773

Bovensmann, H., Burrows, J. P., Buchwitz, M., Frerick, J., Noël, S., Rozanov, V. V., Chance, K. V., and Goede, A.: SCIAMACHY – mission objectives and measurement modes, J. Atmos. Sci., 56, 127–150, 1999. 4773

AMTD
6, 4769–4850, 2013

Bovensmann, H., Buchwitz, M., Burrows, J. P., Reuter, M., Krings, T., Gerilowski, K., Schneising, O., Heymann, J., Tretner, A., and Erzinger, J.: A remote sensing technique for global monitoring of power plant CO_2 emissions from space and related applications, Atmos. Meas. Tech., 3, 781–811, doi:10.5194/amt-3-781-2010, 2010. 4772, 4773, 4774, 4775, 4776, 4777, 4778, 4779, 4783, 4792, 4796, 4799, 4800

Buchwitz, M., de Beek, R., Burrows, J. P., Bovensmann, H., Warneke, T., Notholt, J., Meirink, J. F., Goede, A. P. H., Bergamaschi, P., Körner, S., Heimann, M., and Schulz, A.: Atmospheric methane and carbon dioxide from SCIAMACHY satellite data: initial comparison with chemistry and transport models, Atmos. Chem. Phys., 5, 941–962, doi:10.5194/acp-5-941-2005, 2005. 4773

Buchwitz, M., Chevallier, F., and Bergamaschi, P.: User Requirements Document (URD) for the GHG-CCI project of ESA's Climate Change Initiative, Technical Report, 45 pp., version 1 (URDv1), 3 February 2011, available at: http://www.esa-ghg-cci.org (last access: 1 February 2013), 2011. 4773

Buchwitz, M., Reuter, M., Schneising, O., Boesch, H., Guerlet, S., Dils, B., Aben, I., Armante, R., Bergamaschi, P., Blumenstock, T., Bovensmann, H., Brunner, D., Buchmann, B., Burrows, J. P., Butz, A., Chédin, A., Chevallier, F., Crevoisier, C. D., Deutscher, N. M., Frankenberg, C., Hase, F., Hasekamp, O. P., Heymann, J., Kaminski, T., Laeng, A., Lichtenberg, G., De Mazière, M., Noël, S., Notholt, J., Orphal, J., Popp, C., Parker, R., Scholze, M., Sussmann, R., Stiller, G. P., Warneke, T., Zehner, C., Bril, A., Crisp, D., Griffith, D. W. T., Kuze, A., O'Dell, C., Oshchepkov, S., Sherlock, V., Suto, H., Wennberg, P., Wunch, D., Yokota, T., and Yoshida, Y.: The Greenhouse Gas Climate Change Initiative (GHG-CCI): comparison and quality assessment of near-surface-sensitive satellite-derived CO_2 and CH_4 global data sets, Remote Sens. Environ., in press, 2013. 4773

Burrows, J. P., Hölzle, E., Goede, A. P. H., Visser, H., and Fricke, W.: SCIAMACHY – scanning imaging absorption spectrometer for atmospheric chartography, Acta Astronaut., 35, 445–451, 1995. 4773

Butz, A., Guerlet, S., Hasekamp, O., Schepers, D., Galli, A., Aben, I., Frankenberg, C,. Hartmann, J.-M., Tran, H., Kuze, A., Keppel-Aleks, G., Toon, G., Wunch, D., Wennberg, P., Deutscher, N., Griffith, D., Macatangay, R., Messerschmidt, J., Notholt, J., and Warneke, T.: Toward accurate CO_2 and CH_4 observations from GOSAT, Geophys. Res. Lett., 38, L14812, doi:10.1029/2011GL047888, 2011. 4774, 4779, 4784

AMTD
6, 4769–4850, 2013

Canadell, J. G., Ciais, P., Dhakal, S., Dolman, H., Friedlingstein, P., Gurney. K. R., Held, A., Jackson, R. B., Le Quéré, C., Malone, E. L., Ojima, D. S., Patwardhan, A., Peters, G. P., and Raupach, M. R.: Interactions of the carbon cycle, human activity, and the climate system: a research portfolio, Curr. Opin. Environ. Sustainabil., 2, 301–311, 2010. 4772

Chevallier, F., Bréon, F.-M., and Rayner, P. J.: Contribution of the orbiting carbon observatory to the estimation of CO_2 sources and sinks: theoretical study in a variational data assimilation framework, J. Geophys. Res., 112, D09307, doi:10.1029/2006JD007375, 2007. 4773

Cogan, A. J., Boesch, H., Parker, R., Feng, L., Palmer, P. I., Blavier, J.-F. L., Deutscher, N., Macatangay, R., Notholt, J., Roehl, C. M., Warneke, T., and Wunch, D.: Atmospheric carbon dioxide retrieved from the greenhouse gases observing satellite: comparison with ground-based TCCON observations and GEOS-Chem model calculations, J. Geophys. Res., 117, D21301, doi:10.1029/2012JD018087, 2012. 4774, 4808

Crisp, D., Atlas, R. M., Bréon, F.-M., Brown, L. R., Burrows, J. P., Ciais, P., Connor, B. J., Doney, S. C., Fung, I. Y., Jacob, D. J., Miller, C. E., O'Brien, D., Pawson, S., Randerson, J. T., Rayner, P., Salawitch, R. S., Sander, S. P., Sen, B., Stephens, G. L., Tans, P. P., Toon, G. C., Wennberg, P. O., Wofsy, S. C., Yung, Y. L., Kuang, Z., Chudasama, B., Sprague, G., Weiss, P., Pollock, R., Kenyon, D., and Schroll, S.: The Orbiting Carbon Observatory (OCO) mission, Adv. Space Res., 34, 700–709, 2004. 4773

Crisp, D., Fisher, B. M., O'Dell, C., Frankenberg, C., Basilio, R., Bösch, H., Brown, L. R., Castano, R., Connor, B., Deutscher, N. M., Eldering, A., Griffith, D., Gunson, M., Kuze, A., Mandrake, L., McDuffie, J., Messerschmidt, J., Miller, C. E., Morino, I., Natraj, V., Notholt, J., O'Brien, D. M., Oyafuso, F., Polonsky, I., Robinson, J., Salawitch, R., Sherlock, V., Smyth, M., Suto, H., Taylor, T. E., Thompson, D. R., Wennberg, P. O., Wunch, D., and Yung, Y. L.: The ACOS CO_2 retrieval algorithm – Part II: Global XCO_2 data characterization, Atmos. Meas. Tech., 5, 687–707, doi:10.5194/amt-5-687-2012, 2012. 4774, 4808

Dlugokencky, E. J., Bruhwiler, L., White, J. W. C., Emmons, L. K., Novelli, P. C., Montzka, S. A., Masarie, K. A., Lang, P. M., Crotwell, A. M., Miller, J. B., and Gatti, L. V.: Observational constraints on recent increases in the atmospheric CH_4 burden, Geophys. Res. Lett., 36, L18803, doi:10.1029/2009GL039780, 2009. 4772

European Space Agency: ESA SP-1313/4, Candidate Earth Explorer Core Missions – Reports for Assessment: FLEX – Fluorscence Explorer, ESA Communication Production Office, Noordwijk, the Netherlands, available at: http://esamultimedia.esa.int/docs/SP1313-4_FLEX.pdf (last access: 1 February 2013), 2008. 4774

AMTD
6, 4769–4850, 2013

Francey, R. J., Trudinger, C. M., van der Schoot, M., Law, R. M., Krummel, P. B., Langenfelds, R. L., L. Steele, L. P., Allison, C. E., Stavert, A. R., Andres, R. J., and Rödenbeck, C.: Atmospheric verification of anthropogenic CO_2 emission trends, Nat. Clim. Change, 3, 520–524, doi:10.1038/nclimate1817, 2013. 4772

Frankenberg, C., Meirink, J. F., van Weele, M., Platt, U., and Wagner, T.: Assessing methane emissions from global spaceborne observations, Science, 308, 1010–1014, 2005. 4778

Frankenberg, C., Butz, A., and Toon, G. C.: Disentangling chlorophyll fluorescence from atmospheric scattering effects in O_2 A-band spectra of reflected sun-light, Geophys. Res. Lett., 38, L03801, doi:10.1029/2010GL045896, 2011. 4781

Frankenberg, C., O'Dell, C., Guanter, L., and McDuffie, J.: Remote sensing of near-infrared chlorophyll fluorescence from space in scattering atmospheres: implications for its retrieval and interferences with atmospheric CO_2 retrievals, Atmos. Meas. Tech., 5, 2081–2094, doi:10.5194/amt-5-2081-2012, 2012. 4777, 4780, 4806

Gerbig, C., Lin, J. C., Wofsy, S. C., Daube, B. C., Andrews, A. E., Stephens, B. B., Bakwin, P. S., and Grainger, C. A.: Toward constraining regional-scale fluxes of CO_2 with atmospheric observations over a continent: 2. analysis of COBRA data using a receptor-oriented framework, J. Geophys. Res., 108, 4757, doi:10.1029/2003JD003770, 2003. 4796

Gerilowski, K., Tretner, A., Krings, T., Buchwitz, M., Bertagnolio, P. P., Belemezov, F., Erzinger, J., Burrows, J. P., and Bovensmann, H.: MAMAP – a new spectrometer system for column-averaged methane and carbon dioxide observations from aircraft: instrument description and performance analysis, Atmos. Meas. Tech., 4, 215–243, doi:10.5194/amt-4-215-2011, 2011.

Guanter, L., Alonso, L., Gómez Chova, L., Meroni, M., Preusker, R., Fischer, J., and Moreno, J.: Developments for vegetation fluorescence retrieval from spaceborne high resolution spectrometry in the O_2 A and O_2 B absorption bands, J. Geophys. Res., 115, D19303, doi:10.1029/2009JD013716, 2010. 4806

Guerlet, S., Basu, S., Butz, A., Krol, M., Hahne, P., Houweling, S., Hasekamp, O. P., and Aben, I.: Reduced carbon uptake during the 2010 Northern Hemisphere summer from GOSAT, Geophys. Res. Lett., doi:10.1002/grl.50402, in press, 2013a. 4772

Guerlet, S., Butz, A., Schepers, D., Basu, S., Hasekamp, O. P., Kuze, A., Yokota, T., Blavier, J.-F., Deutscher, N. M., Griffith, D. W. T., Hase, F., Kyro, E., Morino, I., Sherlock, V., Sussmann, R. S., Galli, A., and Aben. I.: Impact of aerosol and thin cirrus on retrieving

AMTD
6, 4769–4850, 2013

and validating XCO_2 from GOSAT shortwave infrared measurements, J. Geophys, Res., doi:10.1002/jgrd.50332, in press, 2013b. 4774, 4777, 4785

Heimann, M., Koerner, S., Tegen, I., and Werner, M.: The global atmospheric tracer model TM3, Technical Reports 5, Max-Planck Institut für Biogeochemie, available from: http://www.bgc-jena.mpg.de/bgc-systems/pmwiki2/pmwiki.php/Publications/TechnicalReports, last access: May 2013, 31 pp., 2003. 4795

Hess., M., Koepke, P., and Schult, I.: Optical properties of aerosols and clouds: the software package OPAC, B. Am. Meteorol. Soc., 79, 831–844, 1998. 4803

Heymann, J., Schneising, O., Reuter, M., Buchwitz, M., Rozanov, V. V., Velazco, V. A., Bovensmann, H., and Burrows, J. P.: SCIAMACHY WFM-DOAS XCO_2: comparison with CarbonTracker XCO_2 focusing on aerosols and thin clouds, Atmos. Meas. Tech., 5, 1935–1952, doi:10.5194/amt-5-1935-2012, 2012a. 4774, 4790

Heymann, J., Bovensmann, H., Buchwitz, M., Burrows, J. P., Deutscher, N. M., Notholt, J., Rettinger, M., Reuter, M., Schneising, O., Sussmann, R., and Warneke, T.: SCIAMACHY WFM-DOAS XCO_2: reduction of scattering related errors, Atmos. Meas. Tech., 5, 2375–2390, doi:10.5194/amt-5-2375-2012, 2012b. 4774, 4777, 4784

Hungershoefer, K., Breon, F.-M., Peylin, P., Chevallier, F., Rayner, P., Klonecki, A., Houweling, S., and Marshall, J.: Evaluation of various observing systems for the global monitoring of CO_2 surface fluxes, Atmos. Chem. Phys., 10, 10503–10520, doi:10.5194/acp-10-10503-2010, 2010. 4784, 4803, 4807

Joiner, J., Yoshida, Y., Vasilkov, A. P., Yoshida, Y., Corp, L. A., and Middleton, E. M.: First observations of global and seasonal terrestrial chlorophyll fluorescence from space, Biogeosciences, 8, 637–651, doi:10.5194/bg-8-637-2011, 2011. 4781

Kauss, J.: Aerosol-Parametrisierung für Strahlungstransport-Simulationen im ultravioletten bis nahinfraroten Spektralbereich, Diploma Thesis, available from: http://www.iup.uni-bremen.de/sciamachy/NIR_NADIR_WFM_DOAS/kauss_dipl.pdf, University of Bremen, Institute of Environmental Physics, Bremen, Germany, 91 pp., 1998. 4803

Keppel-Aleks, G., Wennberg, P. O., O'Dell, C. W., and Wunch, D.: Towards constraints on fossil fuel emissions from total column carbon dioxide, Atmos. Chem. Phys., 13, 4349–4357, doi:10.5194/acp-13-4349-2013, 2013. 4772, 4795

Kort, E. A., Frankenberg, C. F., Miller, C. E., and Oda, T.: Space-based observations of megacity carbon dioxide, Geophys. Res. Lett., 39, L17806, doi:10.1029/2012GL052738, 2012. 4772, 4792, 4794

AMTD
6, 4769–4850, 2013

Krings, T., Gerilowski, K., Buchwitz, M., Reuter, M., Tretner, A., Erzinger, J., Heinze, D., Pflüger, U., Burrows, J. P., and Bovensmann, H.: MAMAP – a new spectrometer system for column-averaged methane and carbon dioxide observations from aircraft: retrieval algorithm and first inversions for point source emission rates, Atmos. Meas. Tech., 4, 1735–1758, doi:10.5194/amt-4-1735-2011, 2011. 4772, 4778, 4792, 4799

Krings, T., Gerilowski, K., Buchwitz, M., Hartmann, J., Sachs, T., Erzinger, J., Burrows, J. P., and Bovensmann, H.: Quantification of methane emission rates from coal mine ventilation shafts using airborne remote sensing data, Atmos. Meas. Tech., 6, 151–166, doi:10.5194/amt-6-151-2013, 2013. 4772, 4778

Kuze, A., Suto, H., Nakajima, M., and Hamazaki, T.: Thermal and near infrared sensor for carbon observation Fourier-transform spectrometer on the greenhouse gases observing satellite for greenhouse gases monitoring, Appl. Optics, 48, 6716–6733, doi:10.1364/AO.48.006716, 2009. 4773

Leifer, I., Culling, D., Schneising, O., Farrell, P., Buchwitz, M., and Burrows, J. P.: Transcontinental methane measurements: Part 2: Mobile surface investigation of fossil fuel industrial fugitive emissions, Atmos. Environ., 74, 432–441, 2013. 4772

Lin, J. C., Gerbig, C., Wofsy, S. C., Andrews, A. E., Daube, B. C., Grainger, C. A., Stephens, B. B., Bakwin, P. S., and Hollinger, D. Y.: Measuring fluxes of trace gases at regional scales by Lagrangian observations: application to the CO_2 Budget and Rectification Airborne (COBRA) study, J. Geophys. Res., 109, D15304, doi:10.1029/2004JD004754, 2004. 4796

Maksyutov, S., Takagi, H., Valsala, V. K., Saito, M., Oda, T., Saeki, T., Belikov, D. A., Saito, R., Ito, A., Yoshida, Y., Morino, I., Uchino, O., Andres, R. J., and Yokota, T.: Regional CO_2 flux estimates for 2009–2010 based on GOSAT and ground-based CO_2 observations, Atmos. Chem. Phys. Discuss., 12, 29235–29288, doi:10.5194/acpd-12-29235-2012, 2012. 4772

McKain, K., Wofsy, S. C., Nehrkorn, T., Eluszkiewicz, J., Ehleringer, J. R., and Stephens, B. B.: Assessment of groundbased atmospheric observations for verification of greenhouse gas emissions from an urban region, P. Natl. Acad. Sci. USA, 109, 8423–8428, doi:10.1073/pnas.1116645109, 2012. 4794

Meirink, J. F., Eskes, H. J., and Goede, A. P. H.: Sensitivity analysis of methane emissions derived from SCIAMACHY observations through inverse modelling, Atmos. Chem. Phys., 6, 1275–1292, doi:10.5194/acp-6-1275-2006, 2006. 4773

AMTD
6, 4769–4850, 2013

Miller, C. E., Crisp, D., DeCola, P. L., Olsen, S. C., Randerson, J. T., Michalak, A. M., Alkhaled, A., Rayner, P., Jacob, D. J., Suntharalingam, P., Jones, D. B. A., Denning, A. S., Nicholls, M. E., Doney, S. C., Pawson, S., Boesch, H., Connor, B. J., Fung, I. Y., O'Brien, D. O., Salawitch, R. J., Sander, S. P., Sen, B., Tans, P., Toon, G. C., Wennberg, P. O., Wofsy, S. C., Yung, Y. L., and Law, R. M.: Precision requirements for space-based X_{CO_2} data, J. Geophys. Res., 112, D10314, doi:10.1029/2006JD007659, 2007.

National Research Council (NRC) – Committee on Methods for Estimating Greenhouse Gas Emissions, Verifying Greenhouse Gas Emissions: Methods to Support International Climate Agreements, 144 pp., available at: http://www.nap.edu/catalog/12883.html (last access: 1 February 2013), 2010. 4773, 4794

O'Dell, C. W., Connor, B., Bösch, H., O'Brien, D., Frankenberg, C., Castano, R., Christi, M., Eldering, D., Fisher, B., Gunson, M., McDuffie, J., Miller, C. E., Natraj, V., Oyafuso, F., Polonsky, I., Smyth, M., Taylor, T., Toon, G. C., Wennberg, P. O., and Wunch, D.: The ACOS CO_2 retrieval algorithm – Part 1: Description and validation against synthetic observations, Atmos. Meas. Tech., 5, 99–121, doi:10.5194/amt-5-99-2012, 2012. 4774, 4779, 4781, 4785

Olivier, J. G. J., Janssens-Maenhout, G., and Peters, J. A. H. W.: Trends in global CO_2 emissions, 2012 Report, PBL Netherlands Environmental Assessment Agency, The Hague, Joint Research Centre, Ispra, 2012. 4772

Oshchepkov, S., Bril, A., Yokota, T., Morino, I., Yoshida, Y., Matsunaga, T., Belikov, D., Wunch, D., Wennberg, P., Toon, G., O'Dell, C., Butz, A., Guerlet, S., Cogan, A., Boesch, H., Eguchi, N., Deutscher, N., Griffith, G., Macatangay, R., Notholt, J., Sussmann, R., Rettinger, M., Sherlock, V., Robinson, J., Kyrö, E., Heikkinen, P., Feist, D. G., Nagahama, T., Kadygrov, N., Maksyutov, S., Uchino, O., and Watanabe, H.: Effects of atmospheric light scattering on spectroscopic observations of greenhouse gases from space: validation of PPDF-based CO_2 retrievals from GOSAT, J. Geophys. Res., 117, D12305, doi:10.1029/2012JD017505, 2012. 4774

Pillai, D.: Mesoscale simulations and inversions of atmospheric CO_2 using airborne and ground-based data, Ph.D. thesis, Max-Planck-Institut für Biogeochemie, Jena, Germany, 171 pp., 2011. 4796

Pillai, D., Gerbig, C., Marshall, J., Ahmadov, R., Kretschmer, R., Koch, T., and Karstens, U.: High resolution modeling of CO_2 over Europe: implications for representation errors of satellite retrievals, Atmos. Chem. Phys., 10, 83–94, doi:10.5194/acp-10-83-2010, 2010. 4795

AMTD
6, 4769–4850, 2013

Pillai, D., Gerbig, C., Kretschmer, R., Beck, V., Karstens, U., Neininger, B., and Heimann, M.: Comparing Lagrangian and Eulerian models for CO_2 transport – a step towards Bayesian inverse modeling using WRF/STILT-VPRM, Atmos. Chem. Phys., 12, 8979–8991, doi:10.5194/acp-12-8979-2012, 2012. 4796

FLEX – FLuorescence EXplorer: a remote sensing approach to quantify spatio-temporal variations of photosynthetic efficiency from space, Photosynth. Res., 91, 293–294, 2007. 4774

Rascher, U., Agati, G., Alonso, L., Cecchi, G., Champagne, S., Colombo, R., Damm, A., Daumard, F., de Miguel, E., Fernandez, G., Franch, B., Franke, J., Gerbig, C., Gioli, B., Gómez, J. A., Goulas, Y., Guanter, L., Gutiérrez-de-la-Cámara, Ó., Hamdi, K., Hostert, P., Jiménez, M., Kosvancova, M., Lognoli, D., Meroni, M., Miglietta, F., Moersch, A., Moreno, J., Moya, I., Neininger, B., Okujeni, A., Ounis, A., Palombi, L., Raimondi, V., Schickling, A., Sobrino, J. A., Stellmes, M., Toci, G., Toscano, P., Udelhoven, T., van der Linden, S., and Zaldei, A.: CEFLES2: the remote sensing component to quantify photosynthetic efficiency from the leaf to the region by measuring sun-induced fluorescence in the oxygen absorption bands, Biogeosciences, 6, 1181–1198, doi:10.5194/bg-6-1181-2009, 2009. 4781

Rayner, P. J. and O'Brien, D. M.: The utility of remotely sensed CO_2 concentration data in surface inversions, Geophys. Res. Lett., 28, 175–178, 2001. 4772

Reuter, M., Buchwitz, M., Schneising, O., Heymann, J., Bovensmann, H., and Burrows, J. P.: A method for improved SCIAMACHY CO_2 retrieval in the presence of optically thin clouds, Atmos. Meas. Tech., 3, 209–232, doi:10.5194/amt-3-209-2010, 2010. 4778, 4779

Reuter, M., Bovensmann, H., Buchwitz, M., Burrows, J. P., Connor, B. J., Deutscher, N. M., Griffith, D. W. T., Heymann, J., Keppel-Aleks, G., Messerschmidt, J., Notholt, J., Petri, C., Robinson, J., Schneising, O., Sherlock, V., Velazco, V., Warneke, T., Wennberg, P. O., and Wunch, D.: Retrieval of atmospheric CO_2 with enhanced accuracy and precision from SCIAMACHY: validation with FTS measurements and comparison with model results, J. Geophys. Res., 116, D04301, doi:10.1029/2010JD015047, 2011. 4774, 4778, 4779

Reuter, M., Bösch, H., Bovensmann, H., Bril, A., Buchwitz, M., Butz, A., Burrows, J. P., O'Dell, C. W., Guerlet, S., Hasekamp, O., Heymann, J., Kikuchi, N., Oshchepkov, S., Parker, R., Pfeifer, S., Schneising, O., Yokota, T., and Yoshida, Y.: A joint effort to deliver satellite retrieved atmospheric CO_2 concentrations for surface flux inversions: the ensemble median algorithm EMMA, Atmos. Chem. Phys., 13, 1771–1780, doi:10.5194/acp-13-1771-2013, 2013.

AMTD
6, 4769–4850, 2013

Rigby, M., Prinn, R. G., Fraser, P. J., Simmonds, P. G., Langenfelds, R. L., Huang, J., Cunnold, D. M., Steele, L. P., Krummel, P. B., Weiss, R. F., O'Doherty, S., Salameh, P. K., Wang, H. J., Harth, C. M., Mühle, J., and Porter, L. W.: Renewed growth of atmospheric methane, Geophys. Res. Lett., 35, L22805, doi:10.1029/2008GL036037, 2008. 4772

Rodgers, C. D.: Inverse Methods for Atmospheric Sounding: Theory and Practice, World Scientific Publishing, River Edge, N.J., 2000. 4779

Rothman, L. S., Gordon, I. E., Barbe, A., Benner, D. C., Bernath, P. E., Birk, M., Boudon, V., Brown, L. R., Campargue, A., Champion, J. P., Chance, K., Coudert, L. H., Dana, V., Devi, V. M., Fally, S., Flaud, J. M., Gamache, R. R., Goldman, A., Jacquemart, D., Kleiner, I., Lacome, N., Lafferty, W. J., Mandin, J. Y., Massie, S. T., Mikhailenko, S. N., Miller, C. E., Moazzen-Ahmadi, N., Naumenko, O. V., Nikitin, A. V., Orphal, J., Perevalov, V. I., Perrin, A., Predoi-Cross, A., Rinsland, C. P., Rotger, M., Simeckova, M., Smith, M. A. H., Sung, K., Tashkun, S. A., Tennyson, J., Toth, R. A., Vandaele, A. C., and Vander Auwera, J.: The HITRAN 2008 molecular spectroscopic database, J. Quant. Spectrosc. Ra., 110, 533–572, doi:10.1016/j.jqsrt.2009.02.013, 2009. 4781

Rozanov, A., Rozanov, V., Buchwitz, M., Kokhanovsky, A., and Burrows, J. P.: SCIATRAN 2.0 – a new radiative transfer model for geophysical applications in the 175–2400 nm spectral region, Adv. Space Res., 36, 1015–1019, doi:10.1016/j.asr.2005.03.012, 2005. 4777, 4779

Rozanov, V. and Kokhanovsky, A.: The solution of the vector radiative transfer equation using the discrete ordinates technique: selected applications, Atmos. Res., 79, 241–265, 2006. 4777, 4779, 4803

Schepers, D., Guerlet, S., Butz, A., Landgraf, J., Frankenberg, C., Hasekamp, O., Blavier, J.-F., Deutscher, N. M., Griffith, D. W. T., Hase, F., Kyro, E., Morino, I., Sherlock, V., Sussmann, R., and Aben, I.: Methane retrievals from Greenhouse Gases Observing Satellite (GOSAT) shortwave infrared measurements: performance comparison of proxy and physics retrieval algorithms, J. Geophys. Res., 117, D10307, doi:10.1029/2012JD017549, 2012. 4778

Schneising, O., Buchwitz, M., Burrows, J. P., Bovensmann, H., Reuter, M., Notholt, J., Macatangay, R., and Warneke, T.: Three years of greenhouse gas column-averaged dry air mole fractions retrieved from satellite – Part 1: Carbon dioxide, Atmos. Chem. Phys., 8, 3827–3853, doi:10.5194/acp-8-3827-2008, 2008. 4772, 4794

Schneising, O., Buchwitz, M., Burrows, J. P., Bovensmann, H., Bergamaschi, P., and Peters, W.: Three years of greenhouse gas column-averaged dry air mole fractions retrieved from satellite – Part 2: Methane, Atmos. Chem. Phys., 9, 443–465, doi:10.5194/acp-9-443-2009, 2009.

AMTD
6, 4769–4850, 2013

Schneising, O., Buchwitz, M., Reuter, M., Heymann, J., Bovensmann, H., and Burrows, J. P.: Long-term analysis of carbon dioxide and methane column-averaged mole fractions retrieved from SCIAMACHY, Atmos. Chem. Phys., 11, 2863–2880, doi:10.5194/acp-11-2863-2011, 2011. 4772, 4778

Schneising, O., Bergamaschi, P., Bovensmann, H., Buchwitz, M., Burrows, J. P., Deutscher, N. M., Griffith, D. W. T., Heymann, J., Macatangay, R., Messerschmidt, J., Notholt, J., Rettinger, M., Reuter, M., Sussmann, R., Velazco, V. A., Warneke, T., Wennberg, P. O., and Wunch, D.: Atmospheric greenhouse gases retrieved from SCIAMACHY: comparison to ground-based FTS measurements and model results, Atmos. Chem. Phys., 12, 1527–1540, doi:10.5194/acp-12-1527-2012, 2012.

Schneising, O., Heymann, J., Buchwitz, M., Reuter, M., Bovensmann, H., and Burrows, J. P.: Anthropogenic carbon dioxide source areas observed from space: assessment of regional enhancements and trends, Atmos. Chem. Phys., 13, 2445–2454, doi:10.5194/acp-13-2445-2013, 2013. 4772, 4792, 4794

Solomon, S., Qin, D., Manning, M., Chen, Z., Marquis, M., Averyt, K. B., Tignor, M., and Miller, H. L. (Eds.): Climate Change 2007: The Physical Science Basis, Contribution of Working Group I to the Fourth Assessment Report of the Intergovernmental Panel on Climate Change (IPCC), Cambridge University Press, 996 pp., 2007. 4772

Stephens, B. B., Gurney, K. R., Tans, P. P., Sweeney, C., Peters, W., Bruhwiler, L., Ciais, P., Ramonet, M., Bousquet, P., Nakazawa, T., Aoki, S., Machida, T., Inoue, G., Vinnichenko, N., Lloyd, J., Jordan, A., Heimann, M., Shibistova, O., Langenfelds, R. L., Steele, L. P., Francey, R. J., and Denning, A. S.: Weak northern and strong tropical land carbon uptake from vertical profiles of atmospheric CO_2, Science, 316, 1732–1735, 2007. 4772

Vasilkov, A., Joiner, J., and Spurr, R.: Note on rotational-Raman scattering in the O_2 A- and B-bands, Atmos. Meas. Tech., 6, 981–990, doi:10.5194/amt-6-981-2013, 2013. 4806

Velazco, V. A., Buchwitz, M., Bovensmann, H., Reuter, M., Schneising, O., Heymann, J., Krings, T., Gerilowski, K., and Burrows, J. P.: Towards space based verification of CO_2 emissions from strong localized sources: fossil fuel power plant emissions as seen by a CarbonSat constellation, Atmos. Meas. Tech., 4, 2809–2822, doi:10.5194/amt-4-2809-2011, 2011. 4772

Winker, D., Vaughan, M., Omar, A., Hu, Y., Powell, K. A., Liu, Z., Hunt, W., and Young, S.: Overview of the CALIPSO mission and CALIOP data processing algorithms, J. Atmos. Ocean. Tech., 26, 2310–2323, 2009. 4790

AMTD
6, 4769–4850, 2013

Wunch, D., Wennberg, P. O., Toon, G. C., Keppel-Aleks, G., and Yavin, Y. G.: Emissions of greenhouse gases from a North American megacity, Geophys. Res. Lett., 36, L15810, doi:10.1029/2009GL039825, 2009. 4794

Yoshida, Y., Ota, Y., Eguchi, N., Kikuchi, N., Nobuta, K., Tran, H., Morino, I., and Yokota, T.: Retrieval algorithm for CO_2 and CH_4 column abundances from short-wavelength infrared spectral observations by the Greenhouse gases observing satellite, Atmos. Meas. Tech., 4, 717–734, doi:10.5194/amt-4-717-2011, 2011. 4773, 4785

Yoshida, Y., Kikuchi, N., Morino, I., Uchino, O., Oshchepkov, S., Bril, A., Saeki, T., Schutgens, N., Toon, G. C., Wunch, D., Roehl, C. M., Wennberg, P. O., Griffith, D. W. T., Deutscher, N. M., Warneke, T., Notholt, J., Robinson, J., Sherlock, V., Connor, B., Rettinger, M., Sussmann, R., Ahonen, P., Heikkinen, P., Kyrö, E., and Yokota, T.: Improvement of the retrieval algorithm for GOSAT SWIR XCO_2 and XCH_4 and their validation using TCCON data, Atmos. Meas. Tech. Discuss., 6, 949–988, doi:10.5194/amtd-6-949-2013, 2013. 4785

AMTD
6, 4769–4850, 2013

Table 1. CarbonSat instrument spectral parameters as used for this study.

Parameter	Spectral band NIR	SWIR-1	SWIR-2	Comment
Spectral range (nm)	747–773	1590–1675	1925–2095	–
Spectral resolution FWHM (nm)	0.1	0.3	0.55	FWHM is the "Full Width at Half Maximum" of the Instrument Spectral Response Function (ISRF)
Spectral Sampling Ratio (SSR) (1/FWHM)	3	3	3	SSR is the number of spectral elements (detector pixel) per spectral resolution FWHM
Signal-to-noise Ratio (SNR) (–)	150 at 3×10^{12}	160 at 1×10^{12}	130 at 3×10^{11}	SNR (per spectral element) given as SNR_{ref} at L_{ref}, where L_{ref} is a reference radiance value in [photon s^{-1} cm^{-2} nm^{-1} sr^{-1}]. Radiance (L) dependence of SNR: $SNR(L) = SNR_{ref} \times \sqrt{L/L_{ref}}$ if $L \geq L_{ref}$ and $SNR(L) = SNR_{ref} \times L/L_{ref}$ if $L < L_{ref}$.

AMTD
6, 4769–4850, 2013

Table 2. BESD/C state vector elements (default settings). The corresponding spectra (columns) of the Jacobian matrix are shown in Fig. 2. For the retrieval the following 3 layers are used: Lower Troposphere (LT, "_00"), Upper Troposphere (UT, "_01"), Stratosphere (ST, "_02"). (*) The a priori surface albedo is obtained via a pre-processing step from the (nearly absorption free) continuum radiance in each band.

No.	ID	Explanation	A priori uncertainty
1	SH_a00	Spectral shift parameter NIR band	0.1 nm
2	SH_b00	Spectral shift parameter SWIR-1 band	0.1 nm
3	SH_c00	Spectral shift parameter SWIR-2 band	0.1 nm
4	SQ_a00	Spectral squeeze/stretch parameter NIR band	0.001 nm nm^{-1}
5	SQ_b00	Spectral squeeze/stretch parameter SWIR-1 band	0.001 nm nm^{-1}
6	SQ_c00	pectral squeeze/stretch parameter SWIR-2 band	0.001 nm nm^{-1}
7	POL_a02	Polynomial coefficient 2 NIR band	1000 (rel.)
8	POL_a01	Polynomial coefficient 1 NIR band	1000 (rel.)
9	POL_a00	Polynomial coefficient 0 NIR band	1000 (rel.)
10	POL_b02	Polynomial coefficient 2 SWIR-1 band	1000 (rel.)
11	POL_b01	Polynomial coefficient 1 SWIR-1 band	1000 (rel.)
12	POL_b00	Polynomial coefficient 0 SWIR-1 band	1000 (rel.)
13	POL_c02	Polynomial coefficient 2 SWIR-2 band	1000 (rel.)
14	POL_c01	Polynomial coefficient 1 SWIR-2 band	1000 (rel.)
15	POL_c00	Polynomial coefficient 0 SWIR-2 band	1000 (rel.)
16	ALB_02	Surface albedo SWIR-2 band	0.05 (rel.(*))
17	ALB_01	Surface albedo SWIR-1 band	0.05 (rel.(*))
18	ALB_00	Surface albedo NIR band	0.05 (rel.(*))
19	CTH_00	Cirrus top height	0.1 (rel.)
20	COD_00	Cirrus optical depth	1.0 (rel.)
21	WOD_00	(Low lying thin) water cloud optical depth	1.0 (rel.)
22	AOD_SW2	AOD SWIR-2 band	0.5 (rel.)
23	AOD_NIR	AOD NIR band	0.5 (rel.)
24	H2O_00	Scaling parameter for water vapor profile	1.0 (rel.)
25	TEM_00	Shift parameter for temperature profile	0.1 (rel.)
26	VCF_00	Scaling factor for Vegetation Chlorophyll Fluorescence	variable (via DVCF retrieval pre-processing)
27	PRE_00	Surface pressure	
28	CH_4_02	Methane sub-column layer ST	0.001 (rel.)
29	CH_4_01	Methane sub-column layer UT	0.005 (rel.)
30	CH_4_00	Methane sub-column layer LT	0.10 (rel.)
31	CO_2_02	CO_2 sub-column layer ST	0.005 (rel.)
32	CO_2_01	CO_2 sub-column layer UT	0.005 (rel.)
33	CO_2_00	CO_2 sub-column layer LT	0.10 (rel.)

AMTD
6, 4769–4850, 2013

Table 3. Description of the three scenarios S1, S2, S3 as used for the Berlin CO_2 emission inversion study. For each scenario the used anthropogenic (fossil fuel) CO_2 emission of Berlin is listed and the resulting XCO_2 enhancement above the XCO_2 background value (see Fig. 12, right panels). The last column reports if the scenario corresponds to a weekday or not. Also listed is the near-surface wind speed (at 240 m; note that the wind speed is similar at other near-surface levels, e.g. 4.70 $m\,s^{-1}$ at 700 m for S1; S2: 7.55 $m\,s^{-1}$; S3: 5.29 $m\,s^{-1}$).

Scenario	Berlin CO_2 emission ($MtCO_2\,yr^{-1}$)	Anthropogenic XCO_2 peak enhancement (ppm)	Comments
S1	54.80	1.47	Weekday, wind speed 4.51 $m\,s^{-1}$
S2	53.89	0.88	Weekday, wind speed 7.44 $m\,s^{-1}$
S3	31.35	0.54	Sunday, wind speed 5.07 $m\,s^{-1}$

AMTD
6, 4769–4850, 2013

Table 4. Results of the Berlin CO_2 emission study. The first column lists the "case" defined by the scenario (S1, S2 or S3; see Table 3), the assumed systematic error of the CarbonSat XCO_2 retrievals ("H0" or "H1"; see below) and the assumed modeling error ("A" or "AB"; see below). The second column lists the used scenario. The third column reports which method has been used to compute the systematic XCO_2 error: the "default" error ("H0") is the error computed via the error parameterization method using the input parameters, e.g. for AOD, as given in the L2e files (see Sect. 6). Because the AOD input parameters are only available at quite low resolution, error "H1" contains an additional aerosol related error which correlates perfectly with the Berlin anthropogenic CO_2 emission plume (worst case scenario; see also Fig. 15). This additional aerosol related error has been computed assuming $\Delta AOD(550\,nm) = 0.2$ per 1 % (4 ppm) ΔXCO_2 enhancement, where ΔXCO_2 is the XCO_2 enhancement relative to the background due to anthropogenic CO_2 emissions. The fourth column lists which assumption has to been used with respect to biogenic XCO_2 modeling errors: "A" means that it is assumed that the spatial pattern (not however the amplitude) of the anthropogenic CO_2 emission plume of Berlin can be accurately modeled in addition to accurate modeling of the spatial XCO_2 pattern due to biogenic emissions; modeling error "AB" assumes the other extreme: here it is assumed that the biogenic pattern cannot be modeled at all resulting in a significant systematic error of the modeling of the spatial XCO_2 pattern. The last two rows list the random and systematic errors of inferred Berlin anthropogenic CO_2 emission derived from a single overpass of CarbonSat over Berlin.

Case	Scenario	Systematic XCO_2 error	Biogenic XCO_2 error	CO_2 emission error	
				random (precision) ($MtCO_2\,yr^{-1}$)	systematic (bias) ($MtCO_2\,yr^{-1}$)
S1_H0_A	S1	default (H0)	no (A)	4.53 (8.3 %)	0.66 (1.2 %)
S1_H1_A	S1	additional aerosol (H1)	no (A)	4.83 (9.0 %)	4.98 (9.1 %)
S1_H1_AB	S1	additional aerosol (H1)	yes (AB)	5.34 (9.7 %)	8.83 (16.1 %)
S2_H0_A	S2	default (H0)	no (A)	6.70 (12.4 %)	−2.18 (−4.0 %)
S2_H1_A	S2	additional aerosol (H1)	no (A)	7.24 (13.4 %)	2.03 (3.8 %)
S2_H1_AB	S2	additional aerosol (H1)	yes (AB)	9.45 (17.5 %)	14.16 (26.3 %)
S3_H0_A	S3	default (H0)	no (A)	5.87 (18.7 %)	3.61 (11.5 %)
S3_H1_A	S3	additional aerosol (H1)	no (A)	6.45 (20.6 %)	6.10 (19.5 %)
S3_H1_AB	S3	additional aerosol (H1)	yes (AB)	4.16 (13.3 %)	−7.75 (−24.7 %)

AMTD
6, 4769–4850, 2013

Table 5. Results of the time series analysis with respect random and systematic errors of the Berlin CO_2 emissions for all 9 cases obtained from analyzing the one year data set of CarbonSat XCO_2 error simulations (detailed results for case S1_H1_A are shown in Fig. 18). The assumed swath width is 240 km. Note that the "Number of good overpasses" is not constant even for a given scenario (e.g. S3). This is because a "good" overpass is determined by the requirement that the uncertainty of the inferred CO_2 emission (as computed via the linear fit of the model to the observations) is required to be less than 25 %. This uncertainty not only depends on the random error of the observations but also on their systematic error.

Case	Number of "good" overpasses	CO_2 emission error (Mean ± Standard Deviation) Random error (precision) ($Mt\,CO_2\,yr^{-1}$)	(%)	Systematic error (bias) ($Mt\,CO_2\,yr^{-1}$)	(%)
S1_H0_A	22	6.5 ± 2.4	11.8 ± 4.4	2.0 ± 2.4	3.6 ± 4.4
S1_H1_A	22	7.1 ± 2.7	13.0 ± 4.9	7.0 ± 2.8	12.7 ± 5.1
S1_H1_AB	18	6.6 ± 2.0	12.0 ± 3.6	8.7 ± 6.4	16.0 ± 11.7
S2_H0_A	19	8.1 ± 2.1	15.0 ± 3.9	0.2 ± 3.0	0.3 ± 5.6
S2_H1_A	17	8.3 ± 1.5	15.3 ± 2.7	4.9 ± 3.8	9.1 ± 7.0
S2_H1_AB	13	9.8 ± 1.9	18.2 ± 3.5	13.5 ± 4.6	25.1 ± 8.6
S3_H0_A	10	6.1 ± 0.9	19.4 ± 2.7	2.2 ± 2.6	7.1 ± 8.2
S3_H1_A	9	6.6 ± 0.8	21.2 ± 2.6	5.4 ± 3.0	17.1 ± 9.5
S3_H1_AB	21	5.3 ± 1.2	17.0 ± 4.0	−9.6 ± 5.1	−30.6 ± 16.4

AMTD
6, 4769–4850, 2013

Table 6. Regional cumulative error distribution results summarizing the percentages of errors less than a given value as shown in Figs. 22 and 23.

Region ID	Region Name	Latitude (deg)	Longitude (deg)	Percentage of XCO_2 retrievals with systematic error		Percentage of XCH_4 retrievals with systematic error	
				< 0.3 ppm	< 0.5 ppm	< 2 ppb	< 4 ppb
USA	USA	+20 – +49	−130 – −70	69.8	99.5	87.7	99.9
EUR	Europe	+35 – +60	−15 – +30	66.7	97.7	81.1	99.7
CHI	China	+20 – +50	+80 – +125	96.2	99.6	99.5	100.0
AUS	Australia	−45 – −10	+110 – +160	99.7	99.9	65.6	100.0
CAN	Canada	+49 – +70	−140 – −50	97.9	100.0	78.3	100.0
SIB	Siberia	+50 – +80	+60 – +130	88.9	99.8	99.4	100.0
AMA	Amazonia	−30 – +15	−90 – −30	97.1	100.0	89.2	100.0
CAF	Central Africa	−20 – +20	−25 – +50	83.6	99.7	60.2	94.5

AMTD
6, 4769–4850, 2013

Table 7. Error parameterization regression functions X0–X7. The "Valid range" indicates the approximate range of values for which the parameterization is valid.

Function	Definition	Explanation	Valid range
X0	1.0	Constant offset	
X1	SZA – 50.0	SZA in [deg]	0–80
X2	ALBN – 0.1	Albedo NIR band [–]	0.03–0.7
X3	ALBS – 0.1	Albedo SWIR-1 band [–]	0.03–0.7
X4	AOD – 0.2	Aerosol Optical Depth at 550 nm [–]	0–0.6
X5	COD – 0.05	Cirrus Optical Depth (NIR) [–]	0–0.6
X6	CTH – 10.0	Cirrus Top Height [km]	2–20
X7	AOD · INC_SZA · INC_ALB	where AOD as for X4 and INC_SZA = cos(84)/cos(SZA+9) · SZA/75 INC_ALB = (1.01/(ALBS+0.01)−1) · 0.01	

AMTD
6, 4769–4850, 2013

Table 8. Error parameterization regression coefficients C0–C7 for the regression functions listed in Table 7, each corresponding to one of the 10 parameterized quantities Q. Row CO_2_RE (CH_4_RE) contains the coefficients for the XCO_2 (XCH_4) random error. Row CO_2_SE (CH_4_SE) contains the coefficients for the XCO_2 (XCH_4) systematic error. Rows AK_CO_2_P0 to AK_CO_2_P2 list the coefficients for the XCO_2 averaging kernel polynomial coefficients P0, P1, and P2. Rows AK_CH_4_P0 to AK_CH_4_P2 list the coefficients for the XCH_4 averaging kernel polynomial coefficients P0, P1, and P2.

Q	C0	C1	C2	C3	C4	C5	C6	C7
CO_2_RE	1.29121	−0.00220	−0.07275	−1.97335	−1.00620	0.34586	−0.00150	38.86071
CO_2_SE	0.30786	0.01191	1.97716	−1.55154	−1.40282	0.70400	−0.03020	−73.46152
CH_4_RE	9.47532	−0.02678	−7.84754	−11.52154	−7.88635	15.80352	0.01702	275.25335
CH_4_SE	1.41086	0.05545	9.17830	−6.77504	−9.15046	5.52796	−0.48784	−335.04555
AK_CO_2_P0	0.25206	−0.00660	−0.97822	1.37264	−0.01718	−0.47370	−0.00132	2.50772
AK_CO_2_P1	1.34678	0.01515	3.96544	−4.98547	0.32270	0.24450	−0.00951	−15.62410
AK_CO_2_P2	−0.60245	−0.00851	−2.98224	3.62314	−0.29681	0.22898	0.01084	12.78807
AK_CH_4_P0	0.93580	−0.01024	−0.68970	−0.13586	0.03922	1.10047	0.00156	−1.59493
AK_CH_4_P1	−0.13742	0.02801	1.88213	0.18662	−0.20388	−2.84238	−0.01870	11.16231
AK_CH_4_P2	0.18796	−0.01763	−1.15321	−0.03191	0.19001	1.68905	0.01708	−10.43191

AMTD
6, 4769–4850, 2013

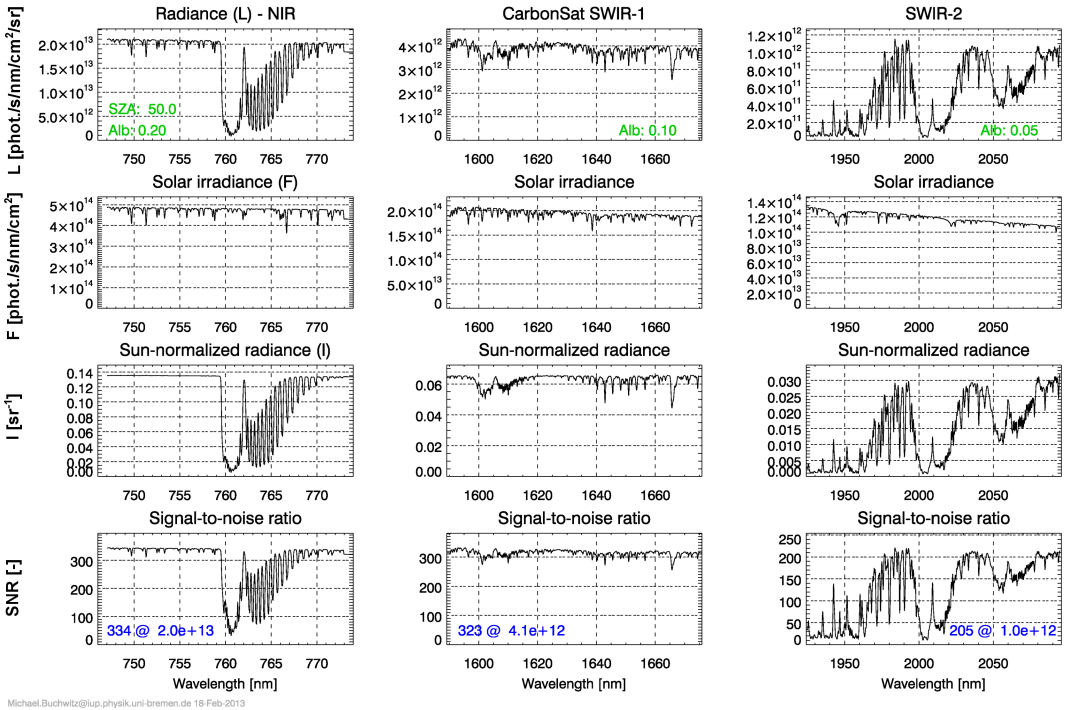

Fig. 1. CarbonSat nadir radiance (top panels), solar irradiance (2nd row), sun-normalized radiance (3rd row) and signal-to-noise ratio (bottom panels) spectra for vegetation albedo and a Solar Zenith Angle (SZA) of 50° ("VEG50 scenario").

AMTD
6, 4769–4850, 2013

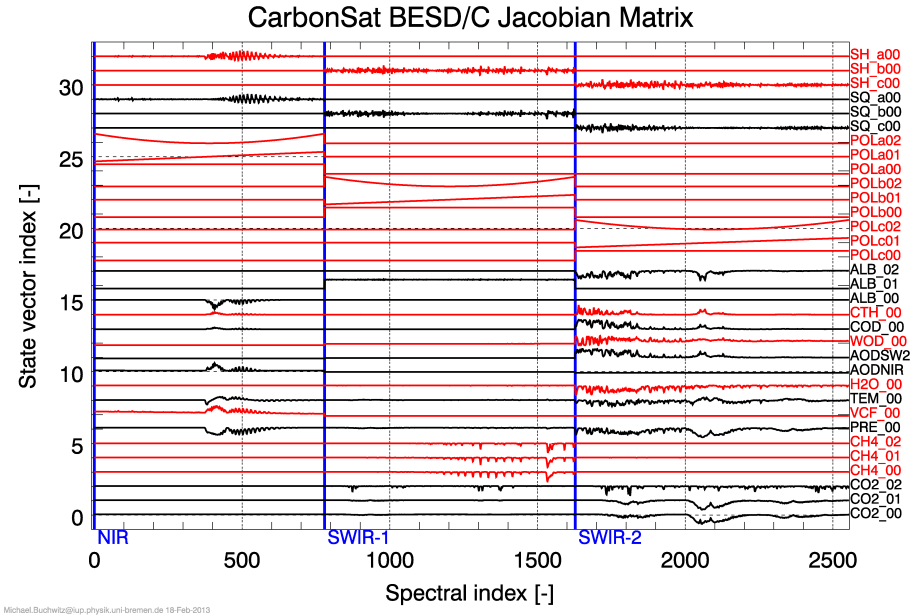

Fig. 2. Typical BESD/C Jacobian matrix. For an explanation of each spectrum (= column of Jacobian matrix) see Table 2.

AMTD
6, 4769–4850, 2013

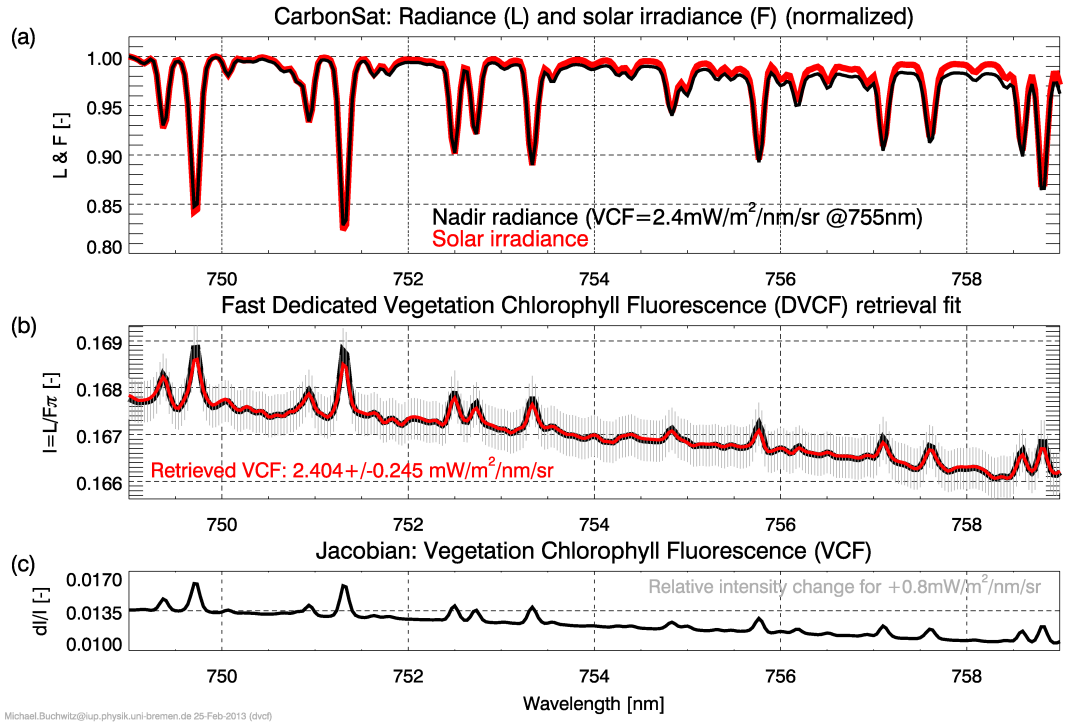

Fig. 3. Illustration of the CarbonSat BESD/C Vegetation Chlorophyll Fluorescence (VCF) pre-processing step. **(a)** Nadir radiance spectrum (L, SZA 40°, vegetation albedo, black line) and solar irradiance (F, red) normalized to their values at 749 nm. The difference is primarily due to VCF emission at the surface of 2.4 $mW\,m^{-2}\,nm^{-1}\,sr^{-1}$ at 755 nm resulting in a difference of the slope and a "filling-in" of the solar Fraunhofer lines (most clearly visible at for the two strong Fraunhofer lines located at 749.7 and 751.3 nm). **(b)** Simulated CarbonSat sun-normalized radiance ($I = L/F \cdot \pi$) measurement (black, with measurement error (grey vertical bars) and fitted VCF Jacobian – red, also shown separately in **(c)**. The retrieved VCF is $2.404 \pm 0.245\,mW\,m^{-2}\,nm^{-1}\,sr^{-1}$ (1-sigma).

AMTD
6, 4769–4850, 2013

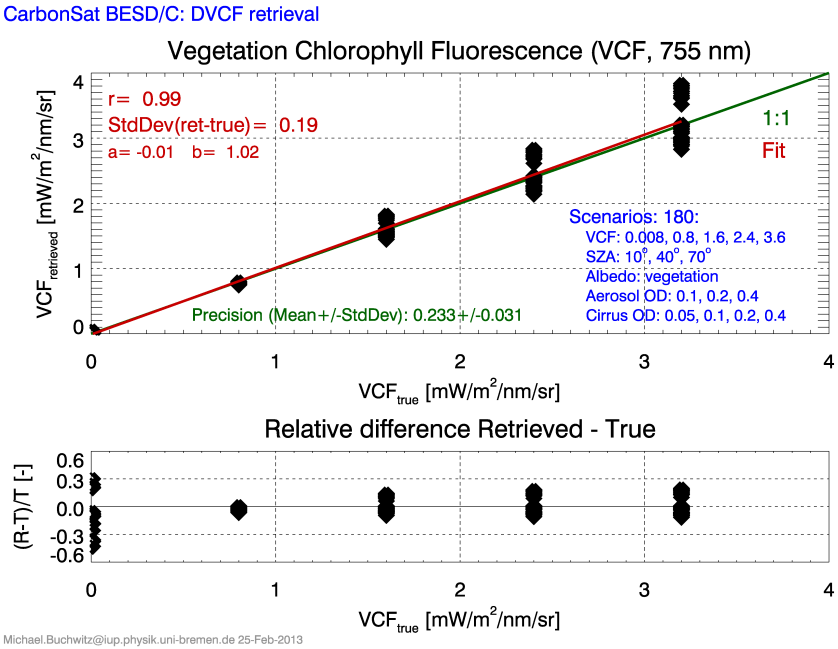

Fig. 4. Results of the Dedicated VCF (DVCF) retrieval pre-processing step. Top: Retrieved VCF (y-axis) versus true VCF (x-axis) for 180 difference scenarios as defined by VCF emission, SZA and aerosol and cirrus optical depth (see blue text for details). The linear correlation coefficient between the retrieved and the true VCF is $r = 0.99$. The standard deviation of the difference between the retrieved and the true VCF is $0.19\,\mathrm{mW\,m^{-2}\,nm^{-1}\,sr^{-1}}$. The random error (single observation precision) is $0.233\,\mathrm{mW\,m^{-2}\,nm^{-1}\,sr^{-1}}$ on average (standard deviation $0.031\,\mathrm{mW\,m^{-2}\,nm^{-1}\,sr^{-1}}$). Bottom: Relative difference between retrieved and true VCF as a function of the true VCF.

AMTD
6, 4769–4850, 2013

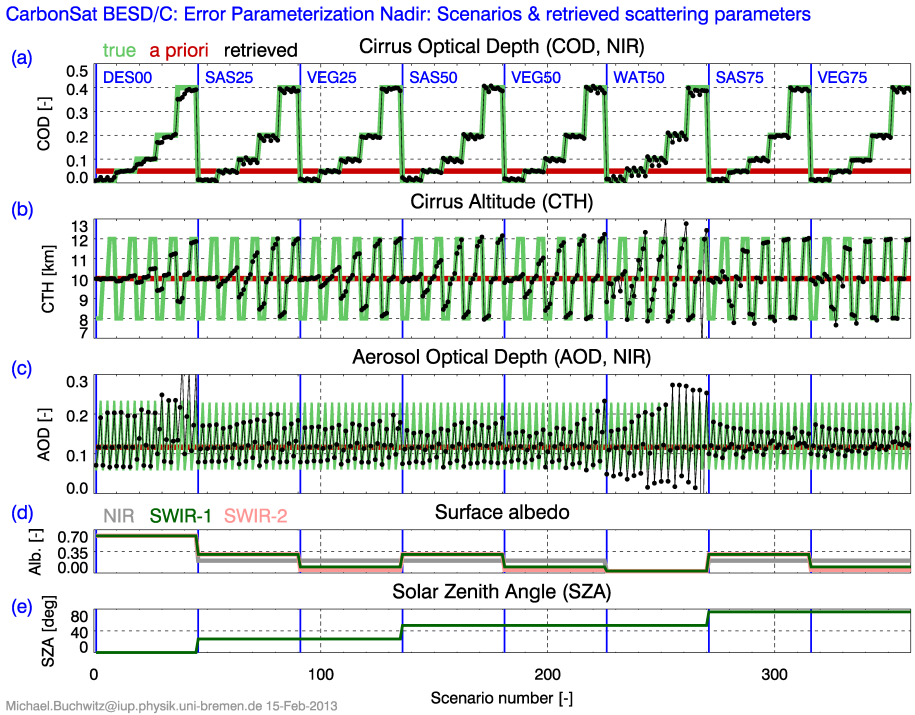

Fig. 5. Scenarios defined for the error parameterization. **(a)** Shows the model atmosphere Cirrus Optical Depth (COD) as green line for all 360 scenarios. The red line shows the a priori COD as used for BESD/C retrieval. The retrieved COD is shown as black line and black dots. Also listed are the scenario identifier indicating surface albedo – DES = desert, SAS = sand/soil, VEG = vegetation, WAT = water; see **(d)** – and Solar Zenith Angle – SZA, 00 = 0°, 25 = 25°, etc.; see **(e)**. **(b)** As **(a)** but for Cirrus Altitude (Cloud Top Height – CTH). **(c)** As **(a)** but for Aerosol Optical Depth (AOD) at 765 nm (NIR band).

AMTD
6, 4769–4850, 2013

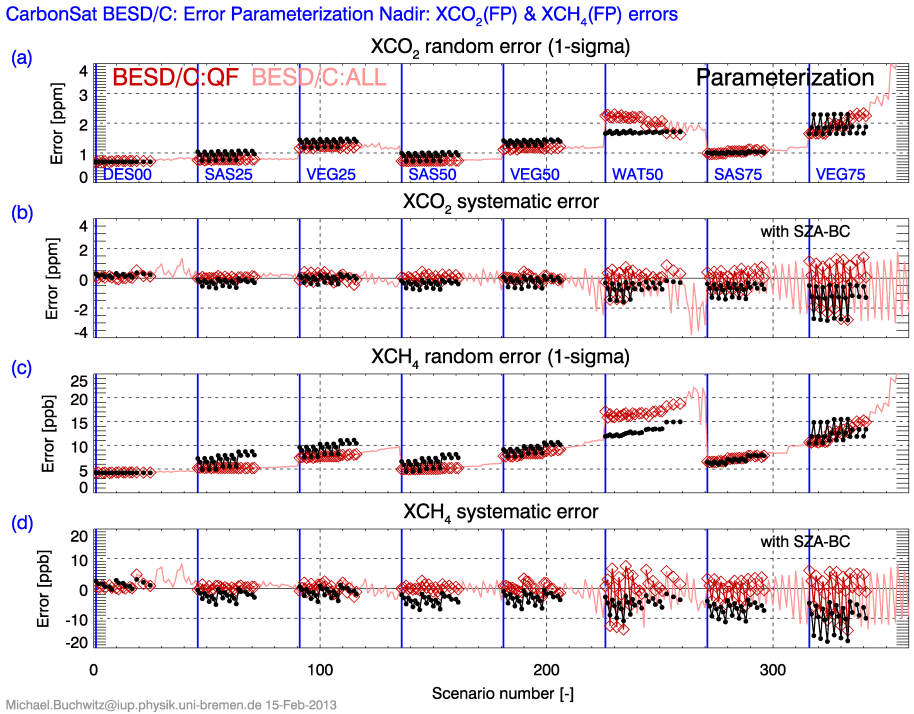

Fig. 6. BESD/C retrieval and error parameterization results. Shown are the unfiltered BESD/C results for all 360 scenarios (see Fig. 5) as light red solid line. The quality filtered BESD/C results are shown as red diamonds. The filtered results correspond to those retrievals where the retrieved AOD(NIR) + COD < 0.3. To model the quality filtered BESD/C results, an error parameterization scheme has been developed and the corresponding results are shown in black. Results are shown for the following parameters: **(a)** XCO_2 random error, **(b)** XCO_2 systematic error, **(c)** XCH_4 random error, and **(d)** XCH_4 systematic error.

AMTD
6, 4769–4850, 2013

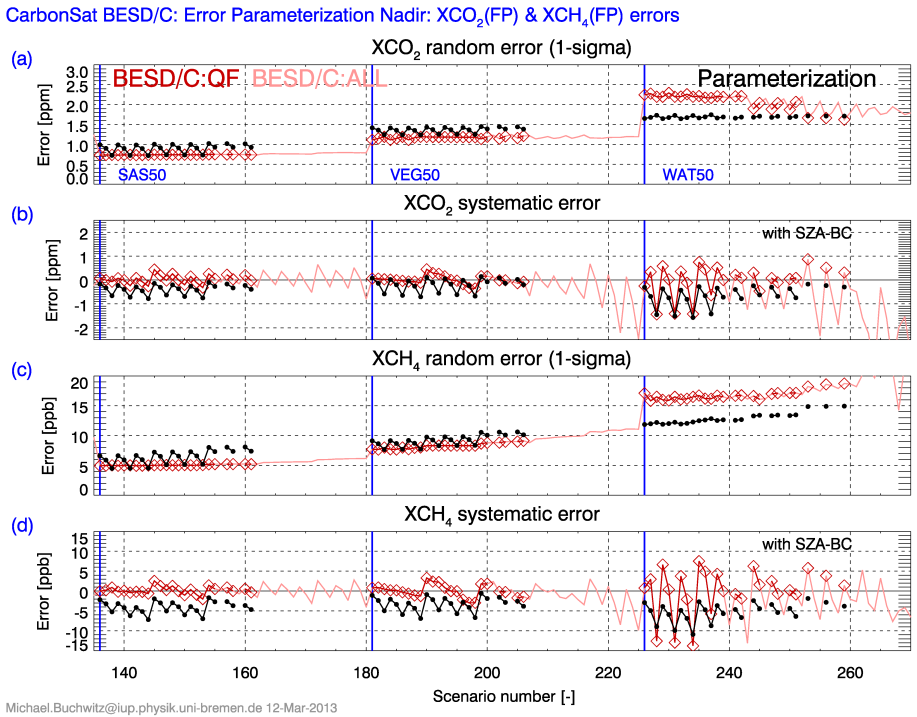

Fig. 7. Zoom into Fig. 6 for the three SZA 50° scenarios corresponding to surface albedos sand/soil (SAS), vegetation (VEG) and water (WAT). As can be seen, the error parameterization tends to overestimate random errors except for very low albedo scenes (WAT), where the random errors are typically underestimated. As can also be seen, the error parameterization tends to produce a low bias (too negative systematic error), especially for the SAS and VEG albedo scenes, and does not capture the full variability of the biases for very low albedo scenes (WAT).

AMTD
6, 4769–4850, 2013

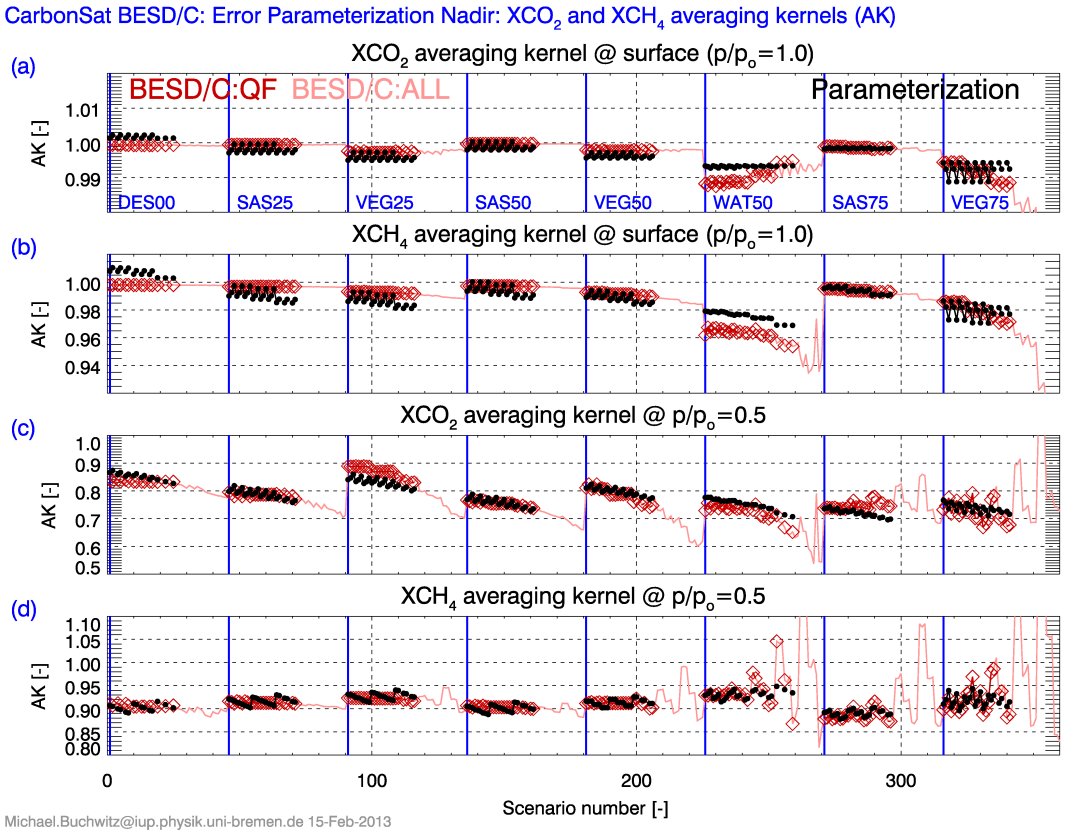

Fig. 8. As Fig. 6 but for the XCO_2 and XCH_4 averaging kernels at $p/p_s = 1.0$ (**a** and **b**) and $p/p_s = 0.5$ (**c** and **d**), where p is the pressure level (altitude) and p_s is surface pressure.

AMTD
6, 4769–4850, 2013

Carbon Monitoring Satellite (CarbonSat)

M. Buchwitz et al.

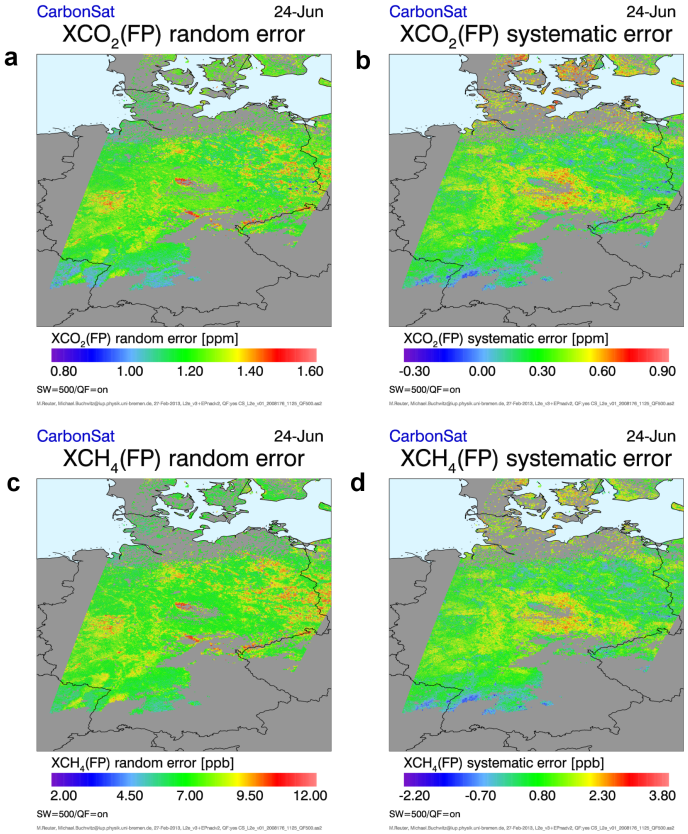

Fig. 9. XCO_2 and XCH_4 random (**a** and **c**) and systematic (**b** and **d**) retrieval errors for a single satellite overpass over Germany assuming a swath width of 500 km. Gaps are due to the limited swath width, (thick) clouds and other filtering criteria as explained in the main text. The errors have been computed using the error parameterization scheme. Some of the input data which have been used for computing these errors are shown in Fig. 10.

AMTD
6, 4769–4850, 2013

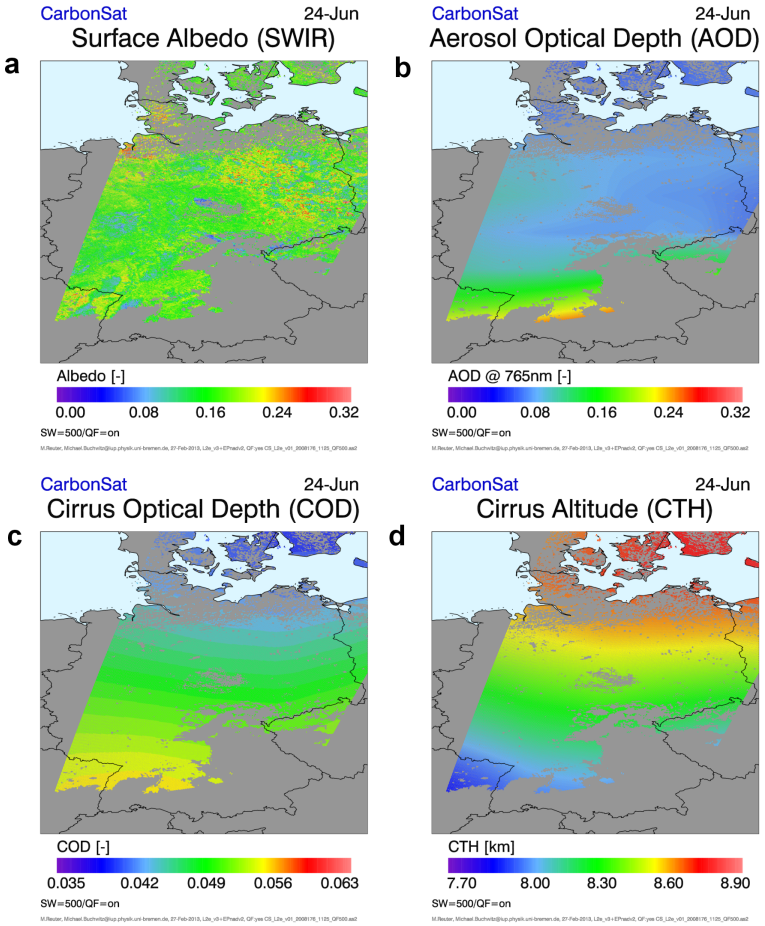

Fig. 10. As Fig. 9 but for the following parameters: **(a)** Surface albedo in the SWIR-1 band, **(b)** AOD in the NIR band, and the cirrus parameters COD **(c)** and CTH **(d)**.

AMTD
6, 4769–4850, 2013

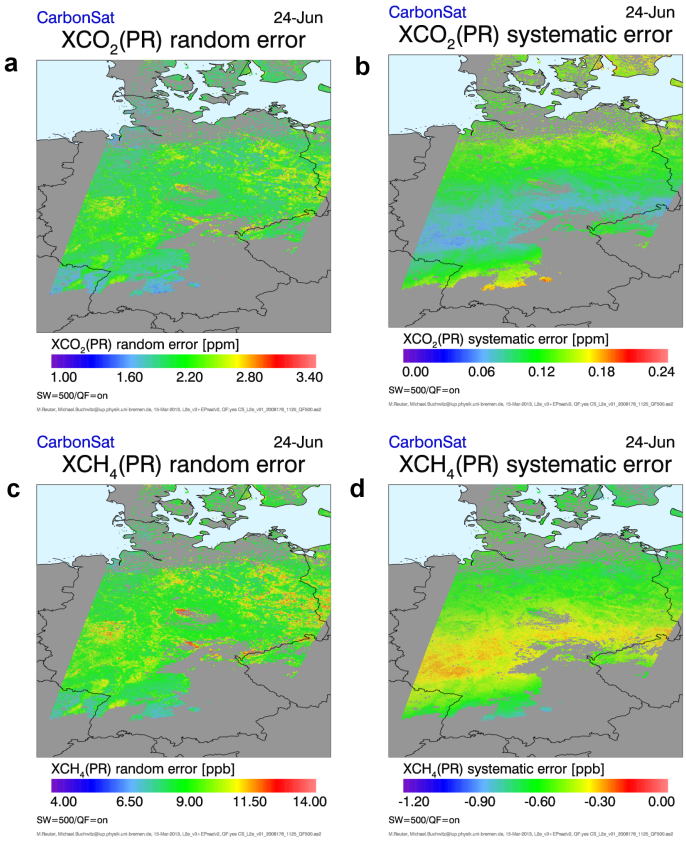

Fig. 11. As Fig. 9 but for "proxy" (PR) retrievals. As can be seen by comparison with Fig. 9, the random errors are larger (as two quite noisy retrievals are combined) but the systematic errors are much smaller, as many errors are common for CO_2 and CH_4 and therefore cancel if the ratio of the retrieved columns is computed.

AMTD
6, 4769–4850, 2013

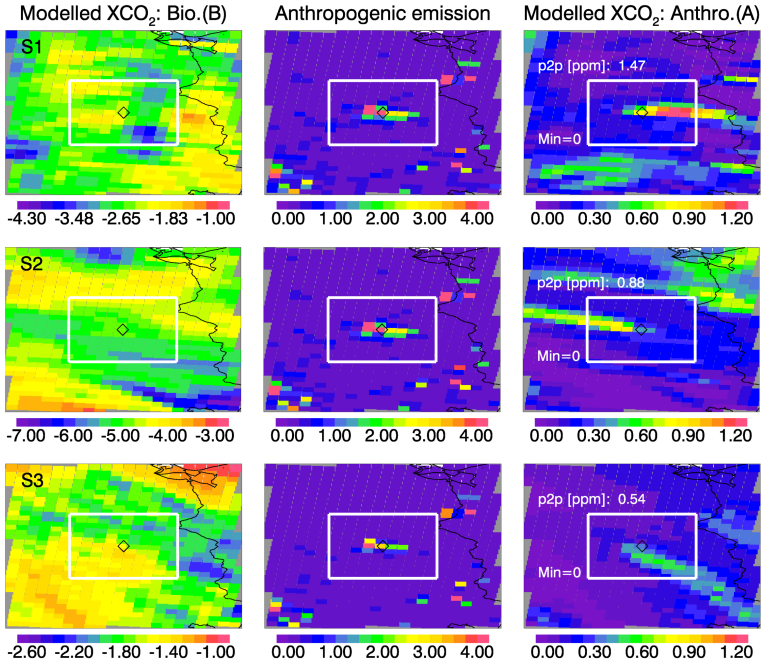

Fig. 12. From left to right: Modeled biospheric XCO_2 component (in ppm), anthropogenic (fossile) CO_2 emissions (in $MtCO_2$ per gridcell and per year, where one grid cell is 10 km × 10 km), and modeled anthropogenic (fossil) XCO_2 component (in ppm; see main text for details). Each row corresponds to a different day in summer around local noon (from top to bottom: "scenario" S1, S2, S3). The days have been selected to represent different conditions (wind speed and direction, CO_2 emissions). The target region used for emission inversion is shown by the white rectangles. The city center of Berlin is indicated by the black diamond located in the center of the target region. Note that for the data shown in the middle and last row the minimum value has been subtracted (i.e. the lowest value in the target region is zero) for better comparison with the inversion results shown in Figs. 14–17.

AMTD
6, 4769–4850, 2013

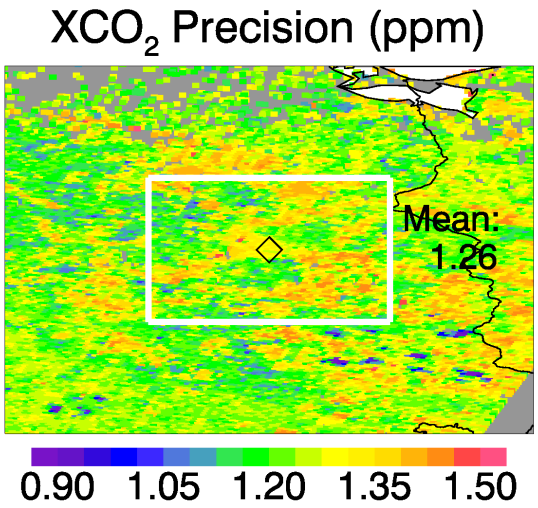

Fig. 13. XCO_2 random error (single measurement precision) around Berlin (zoom in Fig. 9a).

AMTD
6, 4769–4850, 2013

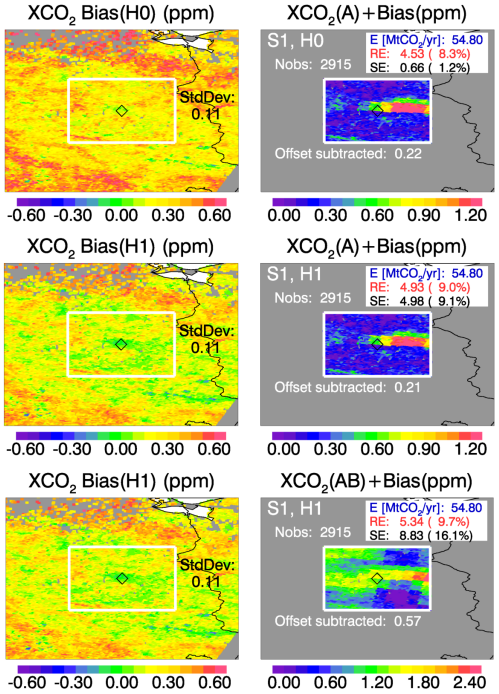

Fig. 14. Inversion results for scenario S1. Top left: CarbonSat XCO_2 systematic error "H0" computed by neglecting additional aerosols correlated with the Berlin CO_2 emission plume. Top right: simulated CarbonSat XCO_2 observation computed as systematic error plus modeled anthropogenic (model "A") XCO_2. Also listed are the number of CarbonSat observations in the target region (Nobs), the anthropogenic CO_2 emission ("E"), and the random error ("RE") and the systematic error ("SE") of the inferred Berlin CO_2 emissions (both in $MtCO_2\,yr^{-1}$ and in percent). Middle row: as top row but for systematic error "H1" computed considering additional aerosols perfectly correlated with the Berlin emission plume. Bottom row: as middle row but assuming that biospheric XCO_2 "disturbs" the inversion but cannot be modeled (model "AB").

AMTD
6, 4769–4850, 2013

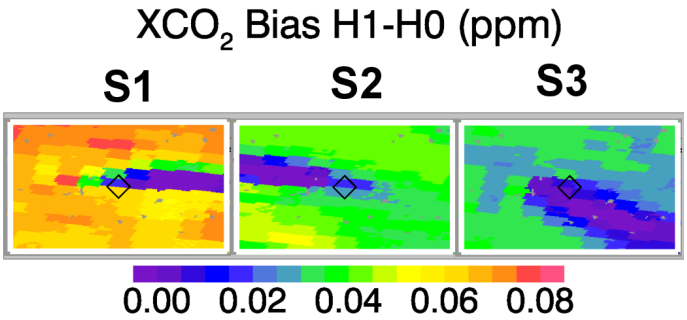

Fig. 15. Difference between systematic errors H1 and H0, i.e. H1–H0 (see Table 4). As can be seen by comparison with the results shown in Figs. 15–17, the bias due to additional aerosols in the Berlin CO_2 emission plume has been computed such that it perfectly correlates with the CO_2 emission plume (worst case). The amplitude of the error is about 0.07 ppm for scenario S1 and about 0.04 ppm for scenarios S2 and S3. Note that for each of the three maps an offset has been subtracted such that the minimum value is zero for each map.

AMTD
6, 4769–4850, 2013

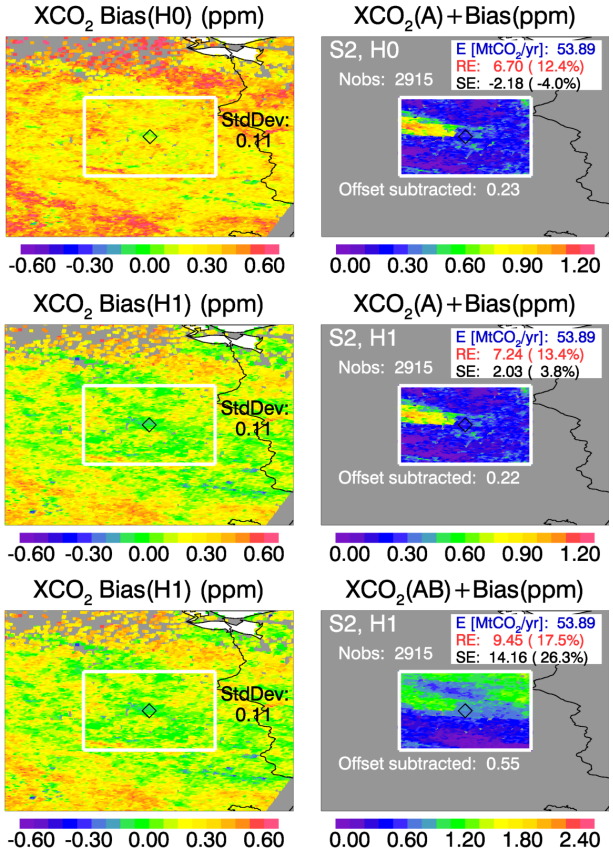

Fig. 16. As Fig. 14 but for scenario S2.

AMTD
6, 4769–4850, 2013

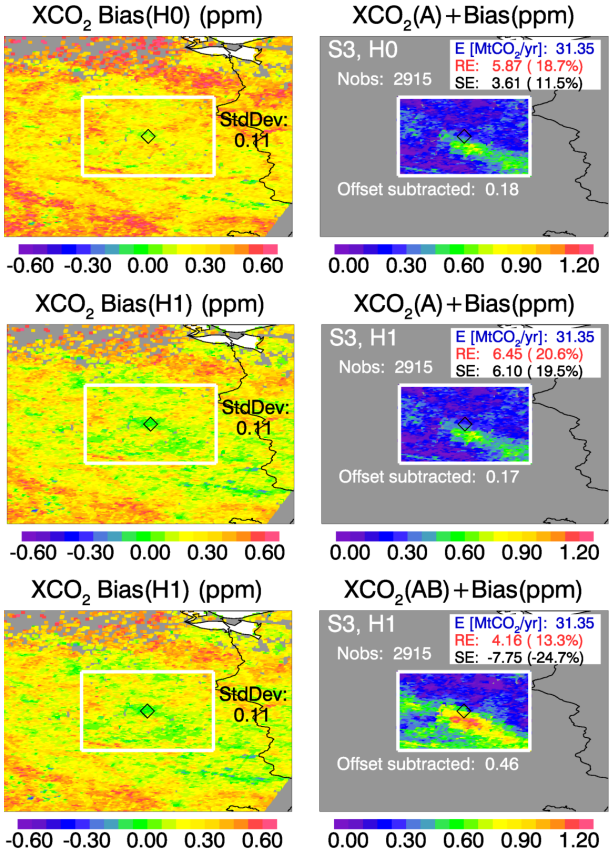

Fig. 17. As Fig. 14 but for scenario S3.

AMTD
6, 4769–4850, 2013

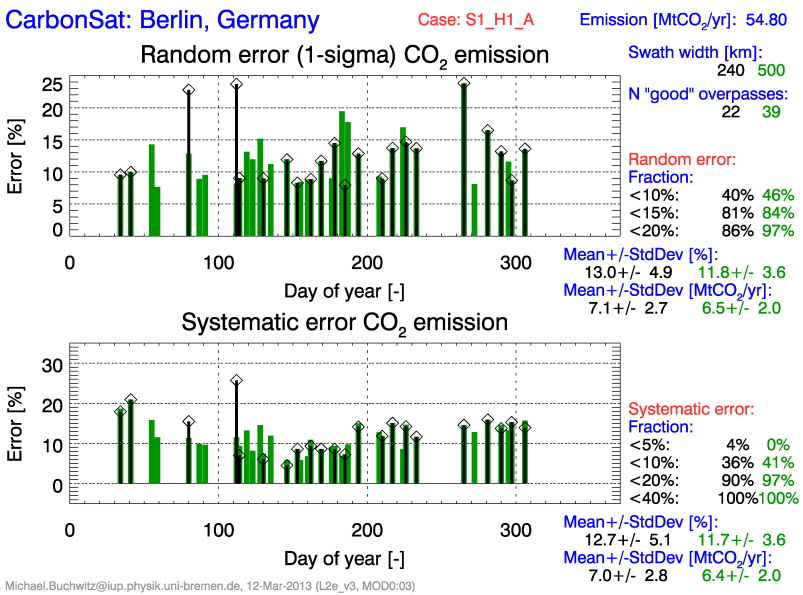

Fig. 18. Estimation of random (top) and systematic (bottom) CO_2 emission errors for CarbonSat Berlin overpasses obtained from analyzing the entire one year data set of simulated CarbonSat XCO_2 retrievals for case S1_H1_A (see Table 4). Shown are the results for a swath width of 240 km (black) and 500 km (green) and for all days (overpasses) where the number of CarbonSat observations at and around the Berlin CO_2 emission plume is sufficiently large to obtain a CO_2 emission random error of less than 25 %. This number is 22 for a swath width of 240 km and 39 for a swath width of 500 km (see "*N* good overpasses"). Also listed are a several figures of merit obtained from a statistical analysis to summarize the results (middle right for the random error; bottom right for systematic error). For example the random error of the inferred emission is less than 20 % for 86 % for all overpasses for a swath width of 240 km. The mean random error is 7.1 $MtCO_2\,yr^{-1}$ (13.0 %) and the standard deviation is 2.7 $MtCO_2\,yr^{-1}$ (4.9 %). Table 5 summarized the results of this analysis for all nine cases.

AMTD
6, 4769–4850, 2013

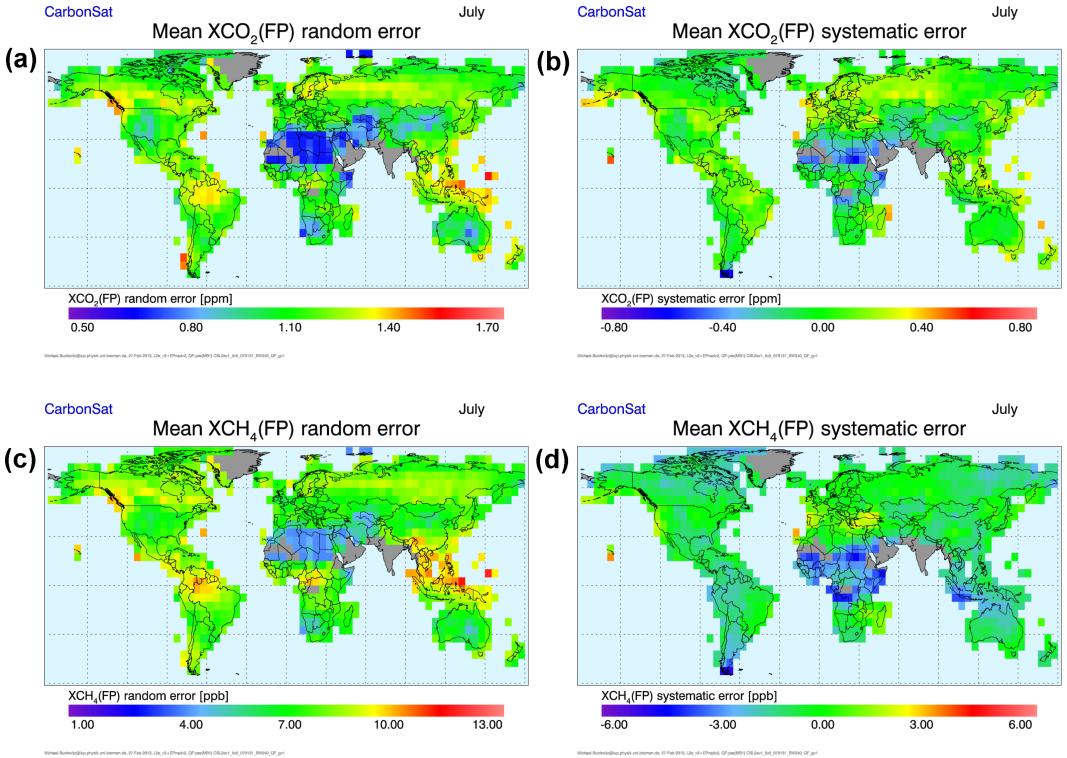

Fig. 19. Spatially averaged (5° × 5°) errors for July for a swath width of 240 km. For this figure all quality-filtered cloud-free observations over snow and ice free land surfaces have been averaged.

AMTD
6, 4769–4850, 2013

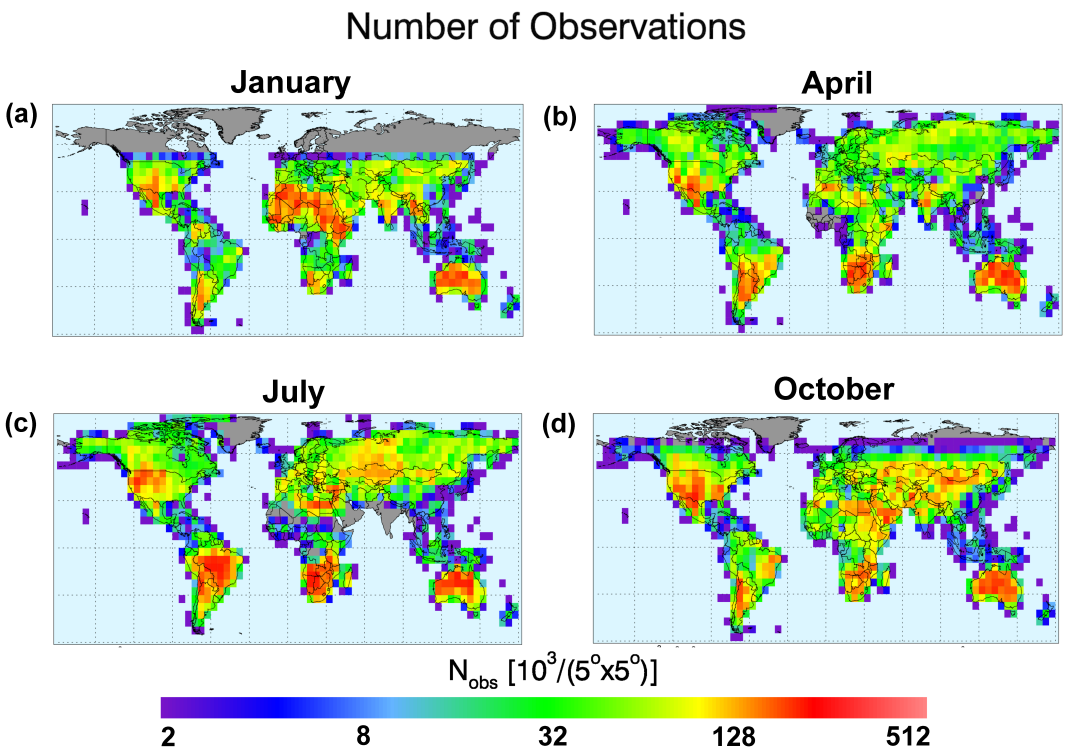

Fig. 20. Number of quality-filtered CarbonSat observations over snow and ice free land surfaces for January **(a)**, April **(b)**, July **(c)** and October **(d)** within each $5^{\circ} \times 5^{\circ}$ grid cell for a swath width of 240 km in units of 1000 observations per grid cell. The total number of observations per month is: 33.15×10^6 for January, 40.40×10^6 for April, 46.28×10^6 for July, and 43.24×10^6 for October.

AMTD
6, 4769–4850, 2013

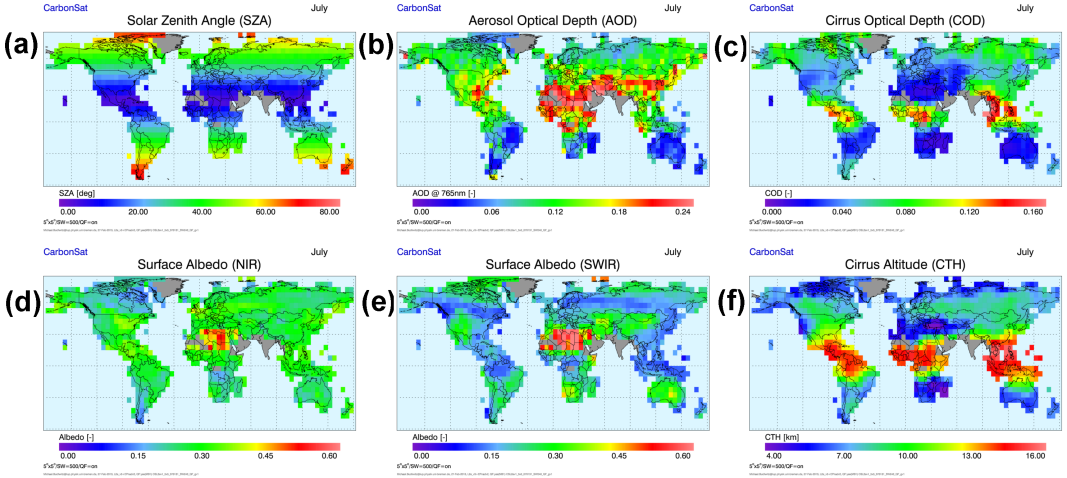

Fig. 21. As Fig. 19 and 20 but for the parameters SZA **(a)**, AOD in the NIR band **(b)**, COD **(c)**, surface albedo in the NIR band **(d)**, surface albedo in the SWIR-1 band **(e)** and CTH **(f)**.

AMTD
6, 4769–4850, 2013

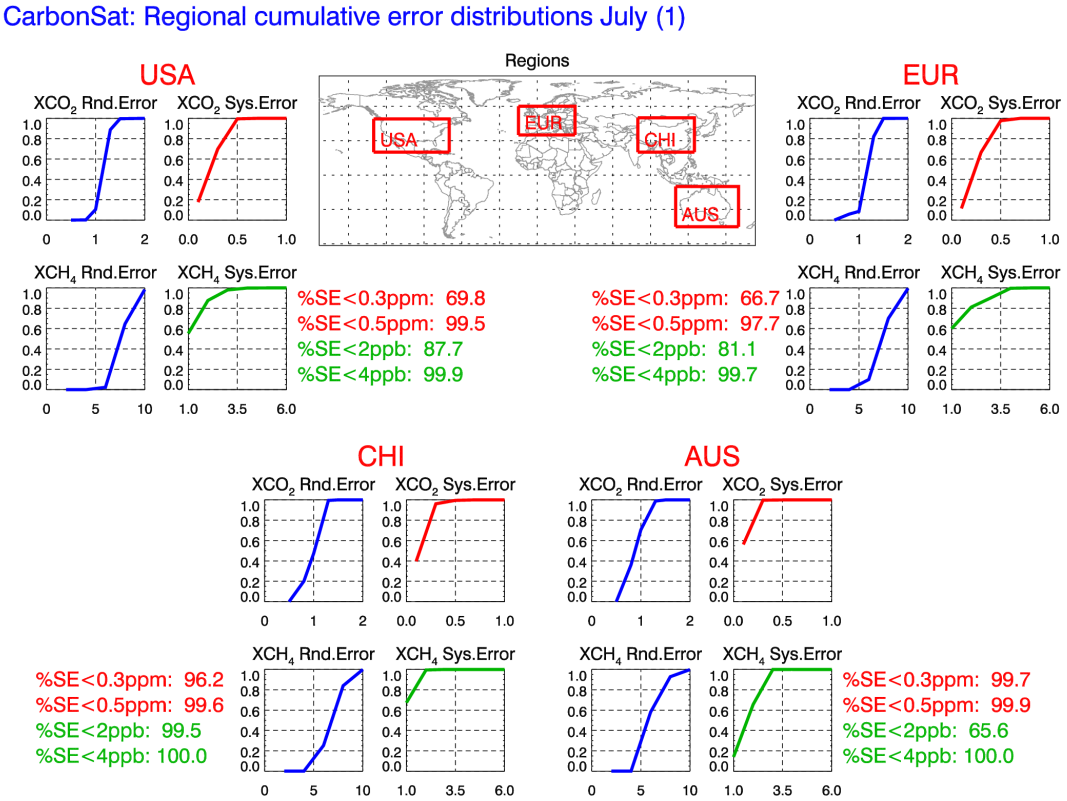

Fig. 22. Regional cumulative error distributions for the four regions United States of America (USA), Europe (EUR), China (CHI) and Australia (AUS) for July. Also listed for each region is the percentage of the individual CarbonSat observations in that region with a systematic error (SE) less than a given value (red for XCO_2, green for XCH_4).

AMTD
6, 4769–4850, 2013

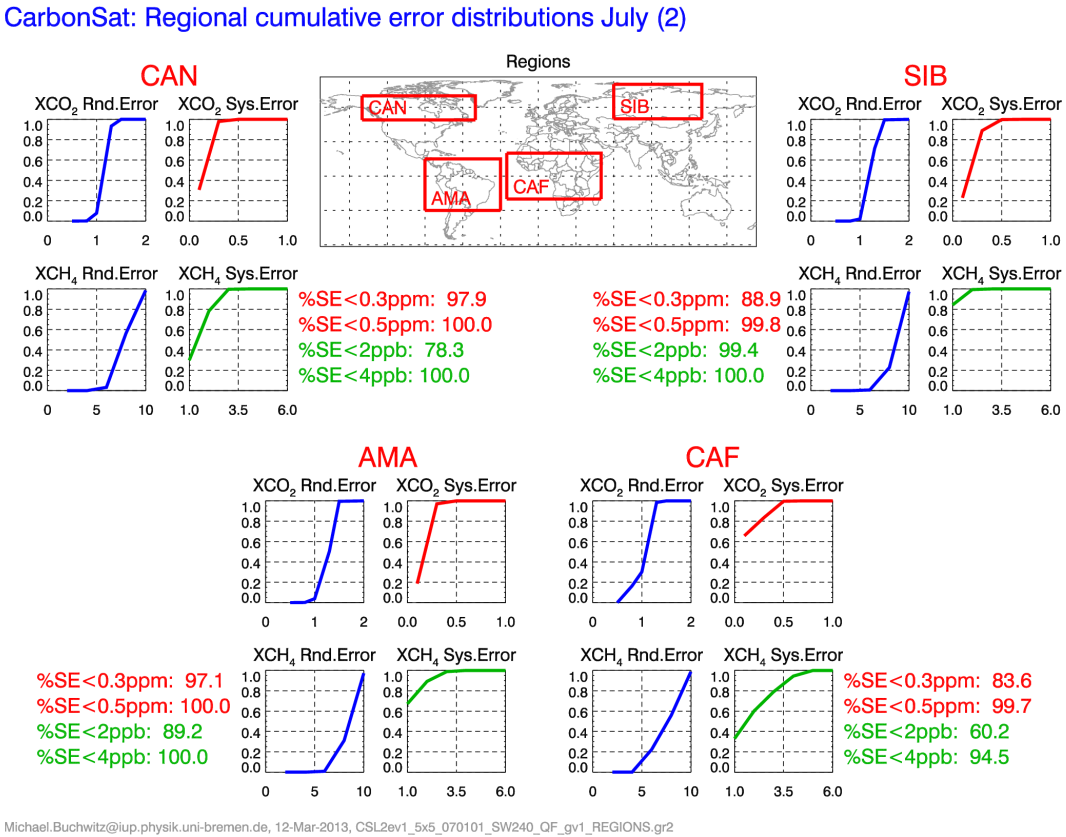

Fig. 23. As Fig. 22 but for the four regions Canada (CAN), Siberia (SIB), Amazonia (AMA) and Central Africa (CAF).

AMTD
6, 4769–4850, 2013